GATOR-GCMM
2. A study of daytime and nighttime ozone layers aloft, ozone in national parks, and weather during the SARMAP field campaign

Mark Z. Jacobson

Department of Civil and Environmental Engineering, Stanford University, Stanford, California

Abstract. The GATORG-GCMM global- through urban-scale nested air pollution/weather forecast model was applied to study ozone layers aloft, ozone in national parks, and weather during the August 3-6, 1990, SARMAP field campaign in northern and central California. Predictions of meteorological variables and mixing ratios of 20 gases were compared with observations. With nesting, the normalized gross error in predicted near-surface Kelvin temperatures was 1.02% and that in near-surface ozone above 50 ppbv was 22.5%. Statistics from outer nested domains indicated that the coarser the grid spacing, the greater the underprediction of ozone. In the absence of nesting, statistics deteriorated but not a lot. The model-simulated observed nighttime ozone layers aloft and daytime ozone mixed layers in the San Joaquin Valley and San Francisco Bay Area. It also simulated observed daytime and nighttime ozone layers aloft over the San Francisco Bay near Hayward. The formation mechanism of these layers is discussed. The model was used to estimate that about 47-57% of peak daytime ozone in Sequoia and Yosemite National Parks during SARMAP was produced by anthropogenic gases, 13-3% was produced by biogenic hydrocarbons, and the rest (about 40%) was background.

1. Introduction

The GATORG-GCMM (gas, aerosol, transport, radiation, general circulation, and mesoscale meteorological) model [*Jacobson*, this issue] was applied to study weather and air pollution during the August 3-6 (Friday-Monday), 1990, SARMAP [San Joaquin Valley air quality study (SJVAQS) and atmospheric utility signatures predictions and experiments study (AUSPEX) regional modeling adaptation project] field campaign in northern and central California [*Lagarias and Sylte*, 1991; *Blumenthal*, 1993; *Ranzieri and Thuillier*, 1994; *Solomon and Thuillier*, 1995]. The model includes nesting from the global through urban scale and treatment of gas, size- and composition-resolved aerosol, radiative, transport, and meteorological processes on all scales.

During the SARMAP study, measurements of over 40 parameters were taken at more than 326 sites. The measurement locations ranged from 34.3°N to 42.4°N and -123.1°W to -117.6°W. Temperatures were measured at 131 sites; relative humidity (RH), 82 sites; winds, 84 sites; air pressures, 6 sites; ozone, 129 sites; nitric oxide, 77 sites; nitrogen dioxide, 77 sites; methane, 18 sites; carbon monoxide, 47 sites; individual organic gases and bond groups, 37 sites. Over 4600 soundings were taken at 44 upper air stations. Sounding data included pressure, temperature, RH, and wind velocities. A detailed characterization of SARMAP measurements can be found in *Solomon and Thuillier* [1995].

The reason the SARMAP data set was chosen for modeling was that it is highly resolved in space and relatively complete with respect to ambient gas and meteorological data and gas emission data. The data set includes more meteorological soundings, aircraft ozone measurements, and surface measurements than were included in the 1987 Southern California Air Quality Study (SCAQS) data set and it covers a larger region than did the SCAQS data set. The organic gas portion of the SARMAP data set is detailed, including 14 organic gases and bond groups. Thus, the data set is ideal for studying organic chemistry in combination with emissions and meteorology. The August 3-6 period of the SARMAP campaign was a period of relatively high ozone mixing ratios in northern California and a period of relatively high pressure and light winds. Thus, the field campaign provided an ideal data set to test the effect of large-scale meteorology on pollution during a typical air pollution event in northern California.

The SARMAP data set has been previously modeled. *Seaman et al.* [1995] used the nonhydrostatic PSU-NCAR mesoscale model MM5 with three nested domains of 4-, 12-, and 36-km resolution, respectively, to test the effects of data assimilation on meteorological predictions. *Lu and Chang* [1998] used the SARMAP air quality model (SAQM) [*Chang et al.*, 1997; *DaMassa et al.*, 1996] to test the effect of indicator species and indicator species ratios as a means of assessing the sensitivity of ozone formation to reductions in precursor emissions. *Dabdub et al.* [1999] used the SAQM to study the effects of boundary conditions on ozone during the SARMAP study. They found that ozone production depended more on influx of nitrogen oxides (NO_x) from regional model boundaries and emissions than on influx or emissions of reactive organic gases (ROGs). *Pun et al.* [2000] assessed model and data needs required for simulating pollution in the SARMAP domain. *T. Umeda and P. T. Martien* [Evaluation of a data assimilation

Table 1. Characteristics of the Nested Domains Used For This Study

Domain	Center Latiude of SW Cell (deg)	Center Longitude of SW Cell (deg)	Number of SN Cells	Number of WE Cells	SN Grid Spacing (deg)	WE Grid Spacing (deg)	Number of Vertical Levels	Top Level (mbar)	Time-Splitting Interval for Gas / Aerosol Procs. (s)	Time-Splitting Interval for Meteorology (s)	Time-Splitting Interval for Radiation (s)	Time-Splitting Interval for Transport (s)	Time-Splitting Interval for Cloud Physics (s)
Global	-87	-180	44	72	4*	5	31	0.425	1800	60	1800	60	1800
Reg 1	10	-180	60	75	1	1	22	100	1800	5	1800	300	1800
Reg 2	22	-143	60	75	0.45	0.45	22	100	1800	5	1800	300	1800
Reg 3	30	-126	60	75	0.20	0.15	22	100	1800	5	1800	300	1800
NCal	36	-123	60	100	0.05	0.05	22	100	1800	4	1800	300	1800
Scal	32.88	-119.35	46	70	0.045	0.05	22	100	1800	5	1800	300	1800

*Six degrees at poles.

technique for a mesoscale meteorological model used for air quality modeling, *J. Appl. Meteorol.*, in review, 2001] used the nonhydrostatic CSU regional atmospheric modeling system (RAMS) with three nested domains coupled with the urban airshed model (UAM-V) in the innermost RAMS domain to study meteorology and ozone during the SARMAP period. They found that ozone predictions appeared to depend more on boundary and initial conditions than on improvements in meteorology obtained from data assimilation.

In this study, a nested global- through urban-scale model is used to study weather and pollution during the SARMAP episode. The goals of the study are to examine elevated ozone, the contribution of anthropogenic and biogenic gases to ozone in Sequoia and Yosemite National Parks, and the ability of the model to predict near-surface and elevated weather and air quality parameters in the presence and absence of nesting.

2. Description of Simulations

Two simulations were run, each from Friday, August 3, 0330 Pacific standard time (PST) (1130 Greenwich mean time) to Monday, August 6, 2330 PST (92-hour simulations). The simulations were run without model spin-up or data
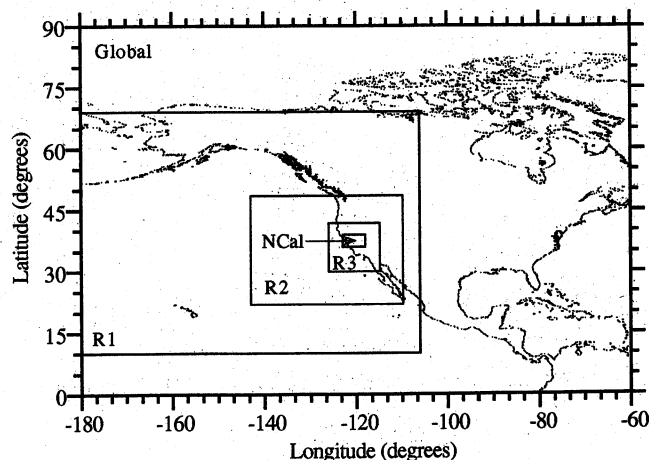
Figure 1. The five nested domains used for this study. The largest domain, "Global," covers the entire Earth. The inner domain, "NCal," covers much of northern and central California. The remaining three domains, "R1," "R2," and "R3,", link the global and urban scales.

assimilation. The simulations included (1) a nested simulation of the global through northern California domains and (2) a simulation of the northern California (innermost) domain alone. Simulations were started with initial interpolated meteorological and gas fields. The time-splitting interval for each process in each domain is given in Table 1. Chemistry was solved with a variable time step, and the time-splitting interval represents the period during which chemistry was integrated alone with variable time steps before another process was solved. The time-splitting interval for nesting from one domain to the next was one-half hour.

The processes accounted for in all domains from the global through urban scale were emissions, gas-phase chemistry, radiative transfer, meteorology, surface processes, species transport, and cloud formation. Aerosol processes were excluded due the lack of a size-segregated aerosol emissions inventory and detailed aerosol observations during this simulation period, but such aerosol processes are included in the model on all scales.

The gas emissions inventory for the SARMAP period was prepared by the California Air Resources Board (CARB) [*Magliano*, 1994]. The inventory domain extended from -123.1° to -118.2°W and from 34.5° to 39.1°N and had a resolution of 0.05° x 0.05°. Emitted gases included NO, NO_2, HONO, CO, HCHO, C_2H_4, and SO_2. Lumped bond groups included olefins, paraffins, seven-carbon aromatics (toluene), eight-carbon aromatics (xylene), high-molecular weight aldehydes, and biogenic hydrocarbons (isoprene). Aerosol parameters included only lumped total sulfate and total aerosol. The inventory, which was limited to northern and central California, was applied to all domains from the global to urban scale. Such treatment did not result in multiple counting of gases in a domain, since coarser domains were used only to provide inflow boundary conditions to finer domains. No information from the part of a coarser domain overlapping a finer domain was fed into the finer domain.

Although additional coarse-resolution (e.g., 1° monthly, seasonally, or yearly averaged) global emission data were available for certain species, the data were not used for three reasons (1) global VOC emission data are not well speciated, so it was expected that ozone predicted from the combined NO_x and VOC global emission data might be in error; (2) the coarse global emission data include too many uncertainties, particularly over cities, to rely on them for calculations in fine grid cells over a short period; and (3) the SARMAP data indicate that near-surface ozone mixing ratios along the

Table 2. Normalized Gross Errors (NGE) and Normalized Biases (NB) for Several Near-Surface Meteorological and Air Quality Parameters From the Nested and Non-nested Simulations

Parameter	Cutoff[a]	No. of Obs.[b]	Innermost Domain (NCal) With Nesting NGE (%)	NB (%)	Second Finest Domain (R3) With Nesting NGE (%)	NB (%)	Third Finest Domain (R2) With Nesting NGE (%)	NB (%)	Largest Regional Domain (R1) With Nesting NGE (%)	NB (%)	Only Domain (Ncal) Without Nesting NGE (%)	NB (%)
Temperature	0 K	8617	1.02	-0.17	1.20	-0.51	1.35	-0.75	1.46	-0.80	1.17	-0.23
Relative humidity	0 %	5597	26.2	-9.2	29.1	0.30	30.2	2.6	29.5	-3.4	29.3	7.3
Wind speed	1.5 m s^{-1}	3534	43.6	-8.5	44.9	-12.5	42.2	-11.8	41.0	-7.0	46.1	-35.7
Wind direction[c]	"	3534	16.9	0.6	17.3	1.6	17.4	1.5	18.7	0.8	17.0	1.2
Air pressure	0 mb	307	0.15	0.10	0.17	0.11	0.38	0.27	0.56	0.30	0.17	-0.10
Ozone (O_3)	50 ppbv	2866	22.5	-8.9	22.9	-5.5	23.4	-6.4	27.4	-17.5	25.3	3.8
Nitric oxide (NO)	0 ppbv	1277	80.2	-32.7	84.4	-27.9	85.8	-29.5	86.4	-27.6	83.2	-54.7
Nitrogen dioxide (NO_2)	0 ppbv	3707	65.9	-13.3	65.5	-7.6	60.8	-11.9	56.7	-24.6	67.8	-48.3
Carbon monoxide (CO)	0 ppbv	2119	49.9	-44.7	48.4	-44.2	52.9	-52.1	61.3	-61.2	37.2	-20.2
Sulfur dioxide (SO_2)	0 ppbv	182	64.3	-63.4	61.9	-61.7	71.6	-71.6	80.4	-80.4	66.3	-53.2
NMOC	0 ppbv	275	48.6	24.6	63.3	44.1	67.6	47.6	72.7	48.2	54.8	-21.3
Methane (CH_4)	0 ppbv	1371	6.4	-2.6	6.4	-2.4	6.4	-2.1	6.5	-2.4	6.7	-2.7
Ethane (C_2H_6)	0 ppbv	275	40.3	4.5	43.1	6.3	45.2	7.0	49.3	12.3	45.3	8.2
Propane (C_3H_8)	0 ppbv	275	49.1	-18.7	52.6	-15.7	57.6	-13.4	61.1	-10.2	52.1	-3.2
Paraffins (PAR)	0 ppbv	275	52.3	25.6	68.9	47	70.4	46.0	70.3	36.4	74.3	64.2
Ethene (C_2H_4)	3 ppbv	45	47.6	7.6	65.3	27.1	50.3	-5.7	43.2	-31.8	57.3	31.3
Olefins (OLE)	0 ppbv	275	53.0	-43.1	54.7	-27.0	62.3	-18.8	70.7	-6.3	55.7	-28.4
Formaldehyde (HCHO)	3 ppbv	33	54.4	37.1	66.4	48.3	75.7	60.4	78.5	69.4	66.1	51.1
Acetaldehyde (CH_3CHO)	2 ppbv	147	37.7	-1.2	48.0	17.8	55.6	27.3	62.1	34.4	51.2	31.1
Acetone (CH_3COCH_3)	1 ppbv	243	33.3	3.4	39.9	10.6	40.9	12.1	39.5	4.2	54.1	35.6
Ketones (KET)	2 ppbv	17	32.4	10.0	32.4	6.2	29.8	-11.6	50.1	-46.0	74.9	61.9
Toluene ($C_6H_5CH_3$)	0 ppbv	275	52.7	-34.2	53.9	-26.0	60.3	-24.4	62.7	-28.9	54.3	-18.3
Xylene ($C_6H_4[CH_3]_2$)	0 ppbv	275	67.8	-62.4	66.8	-57.4	71.0	-54.6	71.4	-54.6	71.3	-55.8
Benzaldehyde ($C_6H_5CH_2O_2$)	0 ppbv	178	47.4	-32.9	46.6	-28.6	47.3	-29.0	48.1	-35.5	59.3	18.2
Isoprene (C_5H_8)	3 ppbv	13	38.5	31.7	124.7	120.9	242.1	229.0	264.3	224.8	48.1	42.1

[a]A cutoff value is the lowest values of the observed parameter considered in the comparison. No. of obs. is the number of observations above the cutoff value. For wind direction, statistics are taken only when the wind speed cutoff is exceeded.
[b]No. obs. is the number of observations in the NCal domain. Comparisons were made only in this domain.
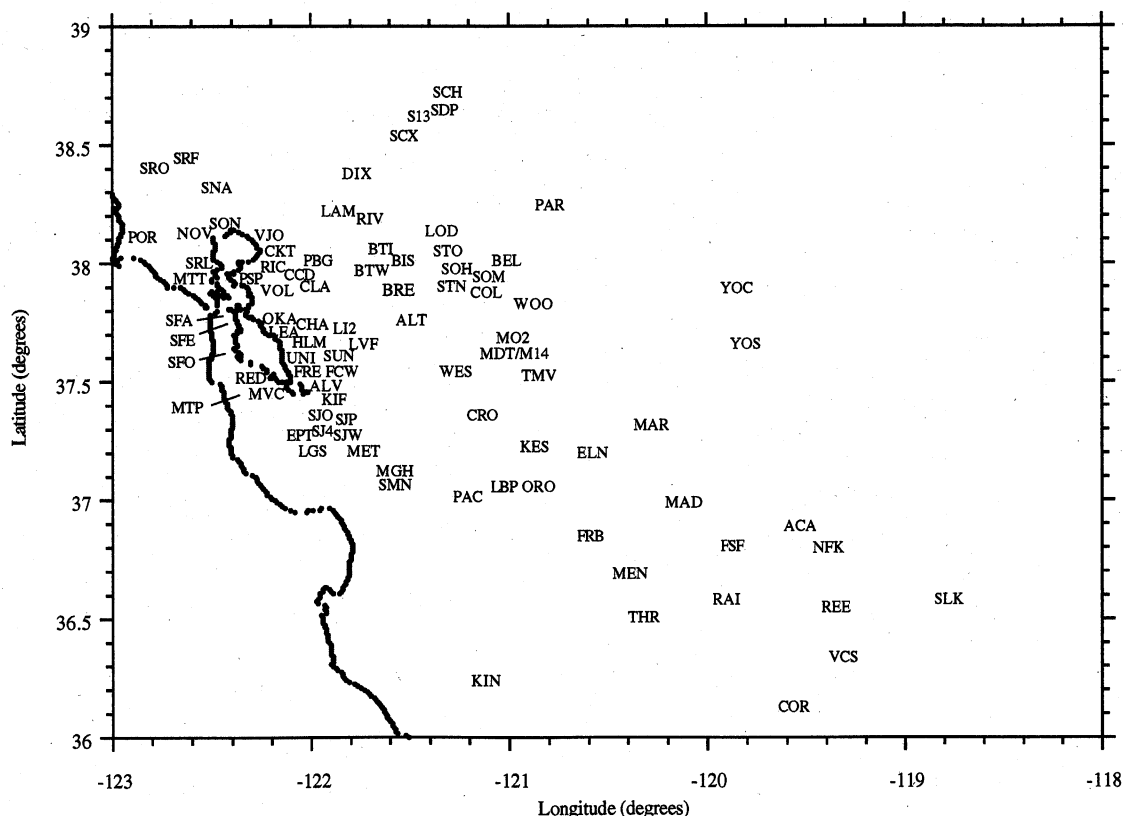[c]Wind direction normalized gross errors are percentages of 360°.

Figure 2. Location of sites at which comparisons with observations are shown for this study.
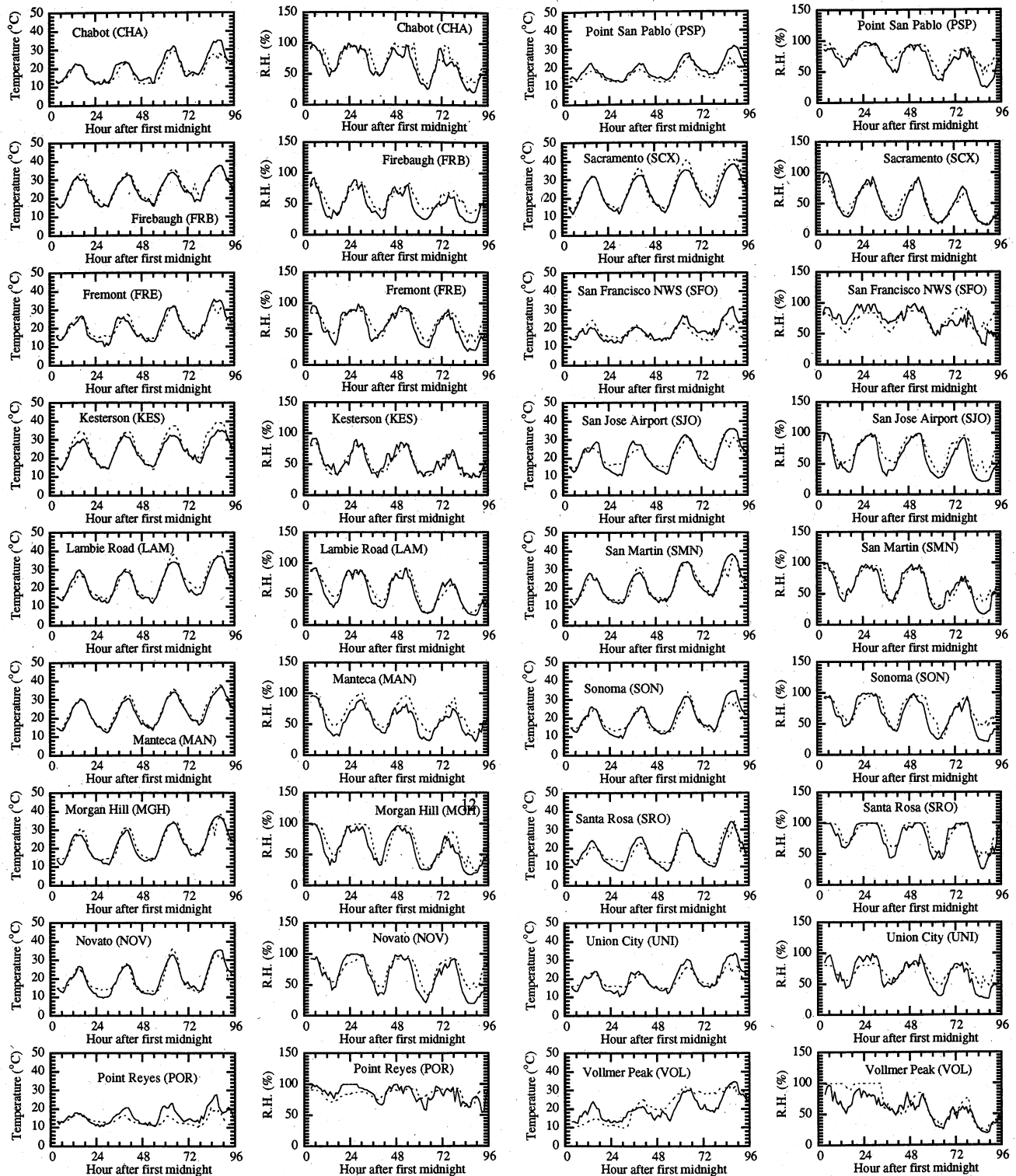
Figure 3. Time series plots, over the 92-hour simulation, of predicted versus observed temperatures and RHs at several locations in the innermost domain during the nested simulation. Solid lines are predictions; dashed lines and circles are observations.

northern California coast were less than or equal to background values all four days of simulation (e.g., Figure 8 for Oakland, Point Reyes, San Francisco); thus, it is unlikely that near-surface ozone was transported in across the California coast during this period. It is possible that elevated ozone was transported in, and this will be the focus of future research.

3. Description of Domains

Five nested domains were used: a global domain, an urban northern California domain, and three regional domains in between. The domains are shown in Figure 1. Table 1 gives statistics about the domain locations, dimensions, and grid
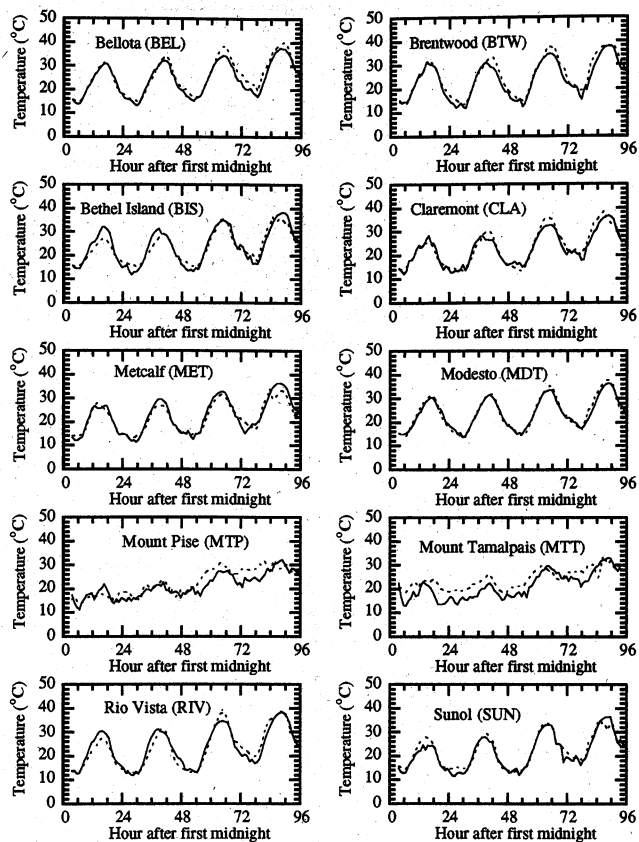
Figure 3. (continued)

spacing. The horizontal and vertical coordinates in all domains were the spherical and sigma-pressure coordinates, respectively. The global domain contained 31 vertical layers between the surface and 0.425 mbar ($\approx$55 km), including 12 layers in the bottom 100 mbar of the model. All regional domains contained 22 vertical layers between the surface and. 100 mbar ($\approx$16 km), and all regional-domain sigma layers exactly matched global-domain sigma layers below the top nine global layers. Thus, the global domain contained nine additional layers above the regional domains.

4. Initial Gas and Meteorological Fields

At the initial time of simulation, an observed 500 mbar height maximum was present over southeastern California. Temperatures at 500 mbar over northern California were relatively high. Winds at 500 mbar were southwesterly and anticyclonic around the high aloft. A 500 mbar height minimum of 5450 m and temperature minimum was present at about 53°N, 150°W (elevated portion of Aleutian low). Winds around the low were cyclonic.
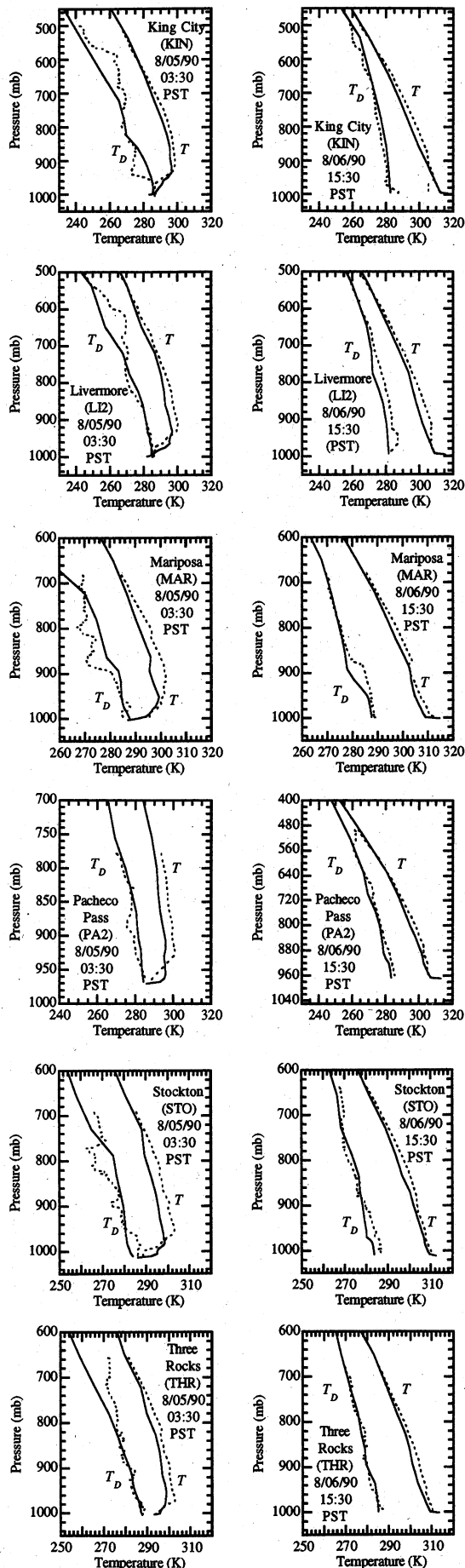
Figure 4. Predicted versus observed vertical profiles of temperature and dew point at several locations at night, after 48 hours of simulation (0330 PST on August 5, 1990), and in the afternoon, after 84 hours of simulation (1530 PST on August 6, 1990). Solid lines are predictions; dashed lines are observations.
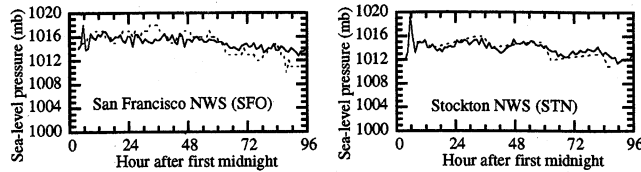
Figure 5. Same as Figure 3 but for air pressure.

Initial meteorological fields in all domains were prepared in the same way. Global 2.5° x 2.5° *National Center for Environmental Prediction (NCEP)* [1999] reanalysis fields for August 3, 1990, at 0400 PST were first interpolated. These fields include temperatures, geopotentials, *u* velocities, and *v* velocities along constant pressure surfaces between 50 and 1000 mbar, and sea surface pressures. Parameters in each NCEP grid cell were first interpolated vertically from NCEP pressure surfaces to a highly resolved (50 m resolution) constant altitude grid. Values from the high-resolution grid were then interpolated horizontally, with bilinear interpolation, to each model column. Column values were then interpolated vertically again from the constant height surfaces to the vertical center of each model grid cell.

Once NCEP fields were interpolated, observed soundings from SARMAP were superimposed over the NCEP-derived values. The initial time of simulation was 0330 PST on August 3, and soundings between 0130 and 0430 PST were used for this interpolation. Sounding data were first interpolated vertically to a high-resolution constant-altitude grid. Values at each high-resolution altitude were then interpolated horizontally to the same high-resolution altitude in each model column with a $1/R^2$ interpolation. Values on each high-resolution surface in the model column were then interpolated to the vertical center of each model grid cell in the column. In order to ensure a smooth transition between the background NCEP fields and the superimposed sounding data, the NCEP fields for each model column were assumed to comprise a virtual sounding a fixed distance away, and the virtual sounding was included in the a $1/R^2$ horizontal interpolation. Thus, if no real sounding data were near a model column, the weighting from the NCEP column dominated. SARMAP surface data were also included in the interpolation.

Soil moisture fields were initialized in the following manner: Within 25 km of the coast, deep soil (0.2-m depth) was initialized with 23% moisture, and surface soil was initialized with 19.6% moisture. Except for soils covered by irrigated cropland (25%), herbaceous wetland (25%), wooded wetland (25%), barren or sparsely vegetated (16%), and rooftops/road surfaces (0%), all other soils were assigned an initial deep soil moisture of 19% (surface soil moisture of 16.2%). The initialization procedure was the same as that in the "baseline" case of *Jacobson* [1999], except that percentages for five specific land use types were also assigned here.

Initial gas fields in all domains were obtained in the following manner: Background gas mixing ratios were first interpolated from latitude-altitude gas mixing ratio fields [e.g., *Jackman et al.*, 1996] and column/point data [e.g., *Singh et al.*, 1996; *Jacob et al.*, 1996; *Bingham et al.*, 1997; *Zhou et al.*, 1997]. Second, SARMAP surface measurements of gas mixing ratios taken near 0330 PST were interpolated to model grid cell horizontal centers in each domain with a $1/R^2$
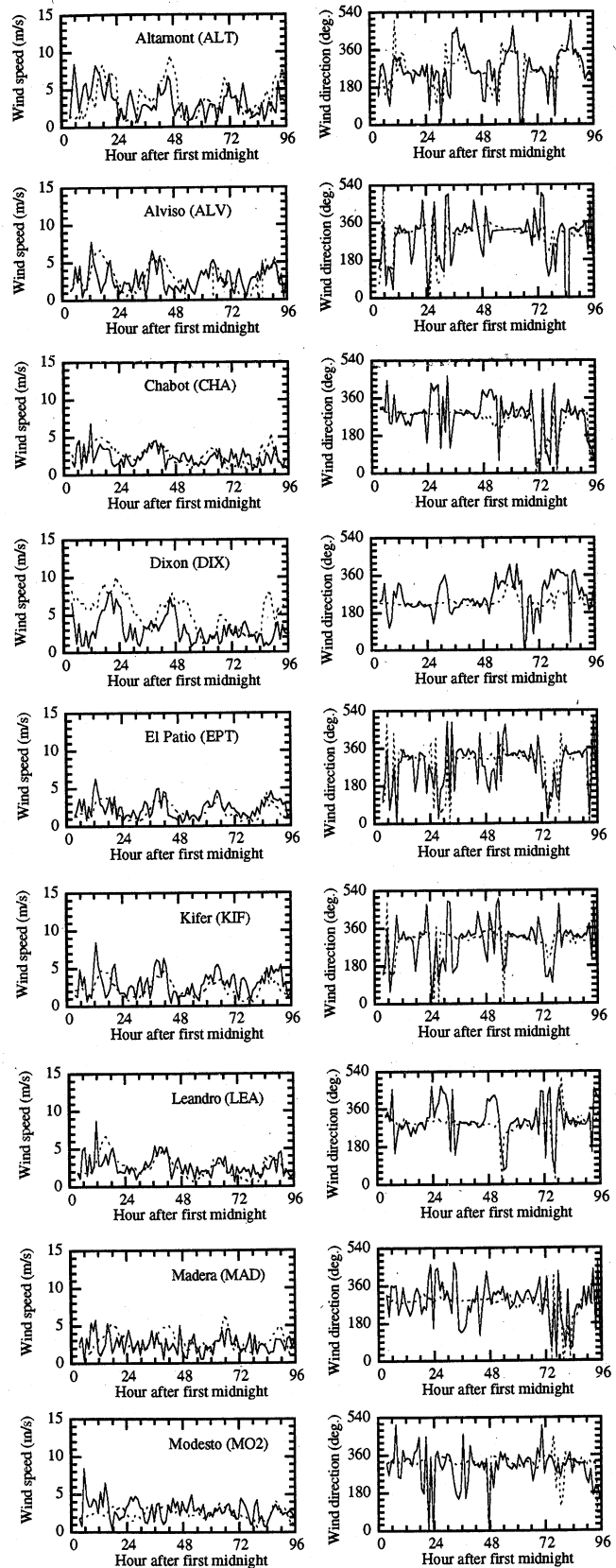

Figure 6. Same as Figure 3 but for wind speed and direction. A wind direction of 0° is a northerly wind (from the north). Directions between 360° and 540° are the same as those between 0° and 180° but used to avoid discontinuities at 360°. Modeled winds are presented at 10-m altitude, the height of the observations.
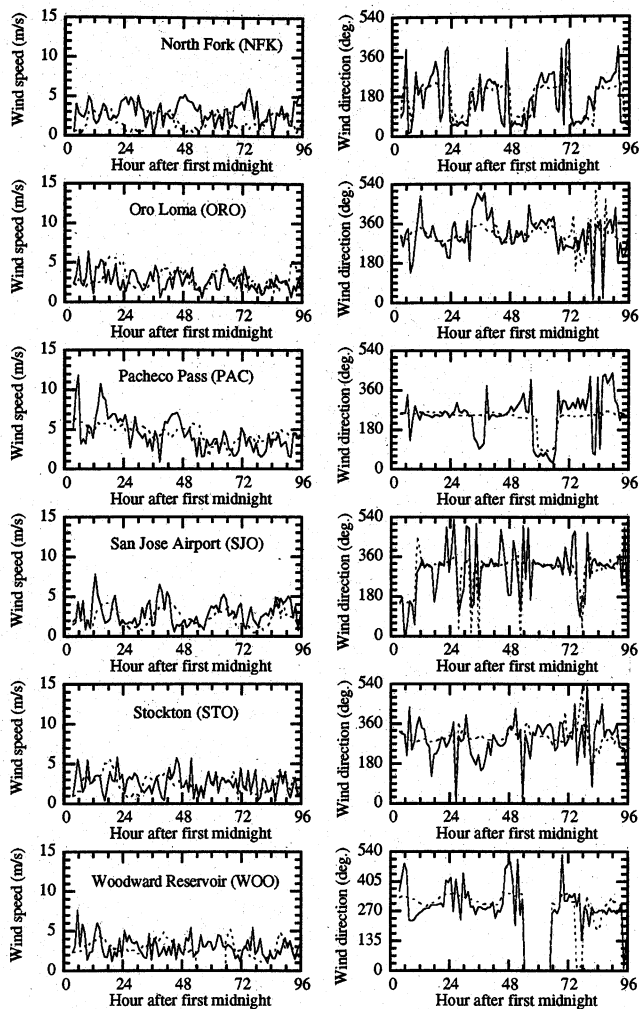
Figure 6. (continued)

domain from the nested simulation. Error statistics, accumulated over the entire simulation period, are shown for all grids in Table 2. In the discussion that follows, the statistics referred to are from the innermost nested domain from the nested simulation. A comparison of nested with nonnested results is discussed in section 6. Figure 2 shows locations of sites referred to in all other figures.
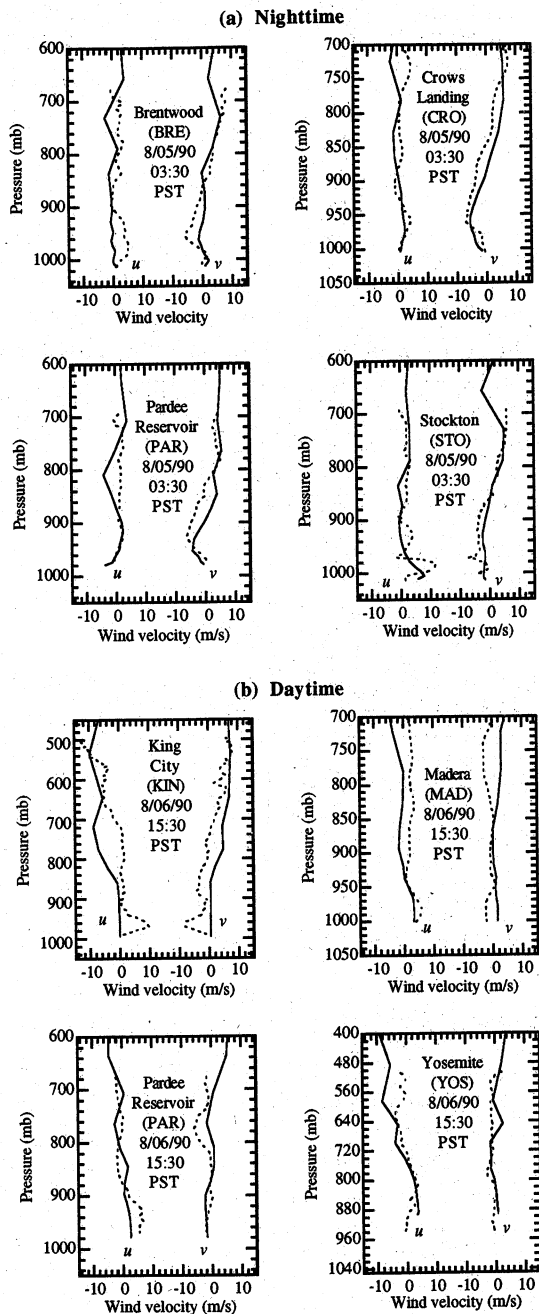
(a) Nighttime

(b) Daytime

interpolation. During the interpolation, the background value in the model cell was also assumed to be an observation point a fixed distance away so that fields in the SARMAP domain gradually merged with background fields. Third, mixing ratios between the surface and 3 km were interpolated. Fourth, aircraft spiral ozone data from SARMAP were interpolated and superimposed over other ozone fields. The spiral data indicate that mixing ratios of ozone in the upper boundary layer during SARMAP exceeded surface values.

Since all domains were initialized in the same way, initial gas distributions in each domain were consistent with each other. This initialization procedure was chosen over spinning up the chemical model, since spin-up results in initial mixing ratios inconsistent with observations at the initial time (as does spin-up of a meteorological model). Spin-up of the chemical model also requires as much computer time as does running the model itself.

5. Results

Model results are first compared with observations for numerous parameters when nesting was used. Time series plots and vertical profile comparisons are shown for many locations. All plots were obtained from the innermost nested

Figure 7. Predicted versus observed vertical profiles of wind speed and direction at several locations at night, after 48 hours of simulation (0330 PST on August 5, 1990), and in the afternoon, after 84 hours of simulation (1530 PST on August 6, 1990). Solid lines are predictions; dashed lines are observations. The lowest modeled velocities shown are those at the middle of the bottom model layer, which varies with location.
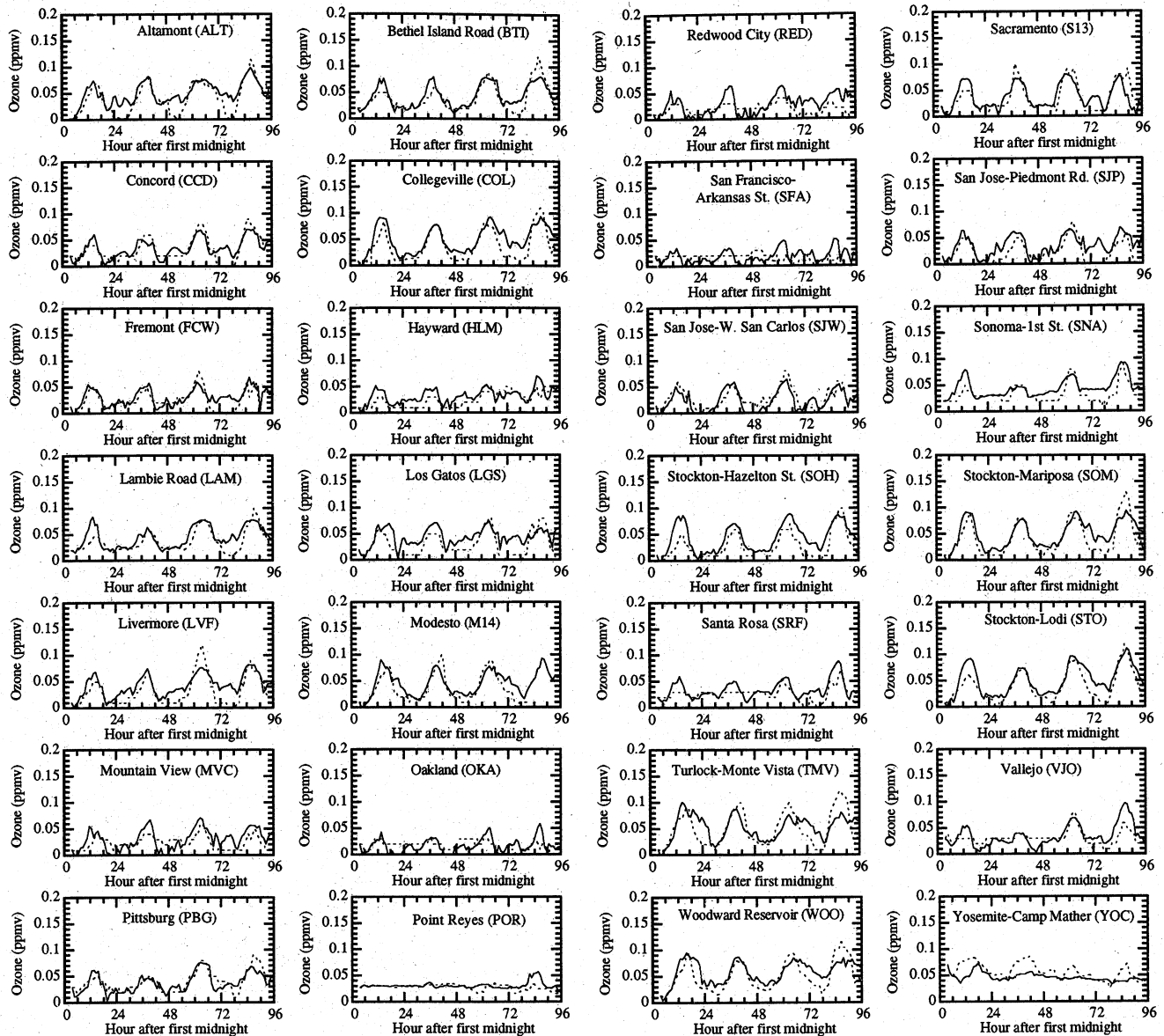
Figure 8. Same as Figure 3 but for ozone.

5.1. Temperature, Relative Humidity, Dew Point

Figure 3 shows time series predictions versus observations of near-surface temperatures and RHs for the 92-hour nested simulation. Table 2 shows that gross errors, normalized over all observations in the NCal domain during the 92-hour period, were 1.02% for Kelvin temperatures and 26.2% for RHs. The RH error is the percent error of the RH value itself; thus, a 25% error of an observed RH of 50% is 12.5% of the RH. Normalized biases indicate slight underpredictions for both parameters.

Figure 3 indicates that the model was able to capture the gradual increases in temperatures and decreases in RHs that occurred each successive day. Temperature variations near the coast are generally weaker than those inland, since coastal areas are exposed to an influx of relatively constant-temperature ocean air, and soil moisture contents near the coast are generally high. RH variations are similarly weaker near the coast than inland due to the weaker temperature

variations and constant source of water vapor near the coast. As shown in Figures 3a and 3b, the model reproduced weak diurnal temperature and RH variations well at near coastal sites, such as Mount Pise (MTP), Mount Tamalpais (MTT), Point Reyes (POR), Point San Pablo (PSP), and San Francisco (SFO). It also reproduced strong diurnal variations of both parameters at inland locations, such as Bellota (BEL), Firebaugh (FRB), Lambie Road (LAM), Lodi (LOD), Manteca (MAN), Modesto (MDT), Morgan Hill (MGH), Novato (NOV), Sacramento (SCX), and San Martin (SMN). The model also captured moderate variations at intermediate locations, such as Fremont (FRE), San Jose (SJO), and Union City (UNI). At three mountainside stations, Mount Tamalpais (MTT), Mount Pise (MTP), and Vollmer Peak (VOL), observed peak temperatures increased by 10°-15°C and observed peak RHs (at Vollmer Peak) decreased by about 40% between the first and the fourth days of simulation. The model captured these trends at all three locations. Temperature prediction accuracy depends significantly on initialization of meteorological variables
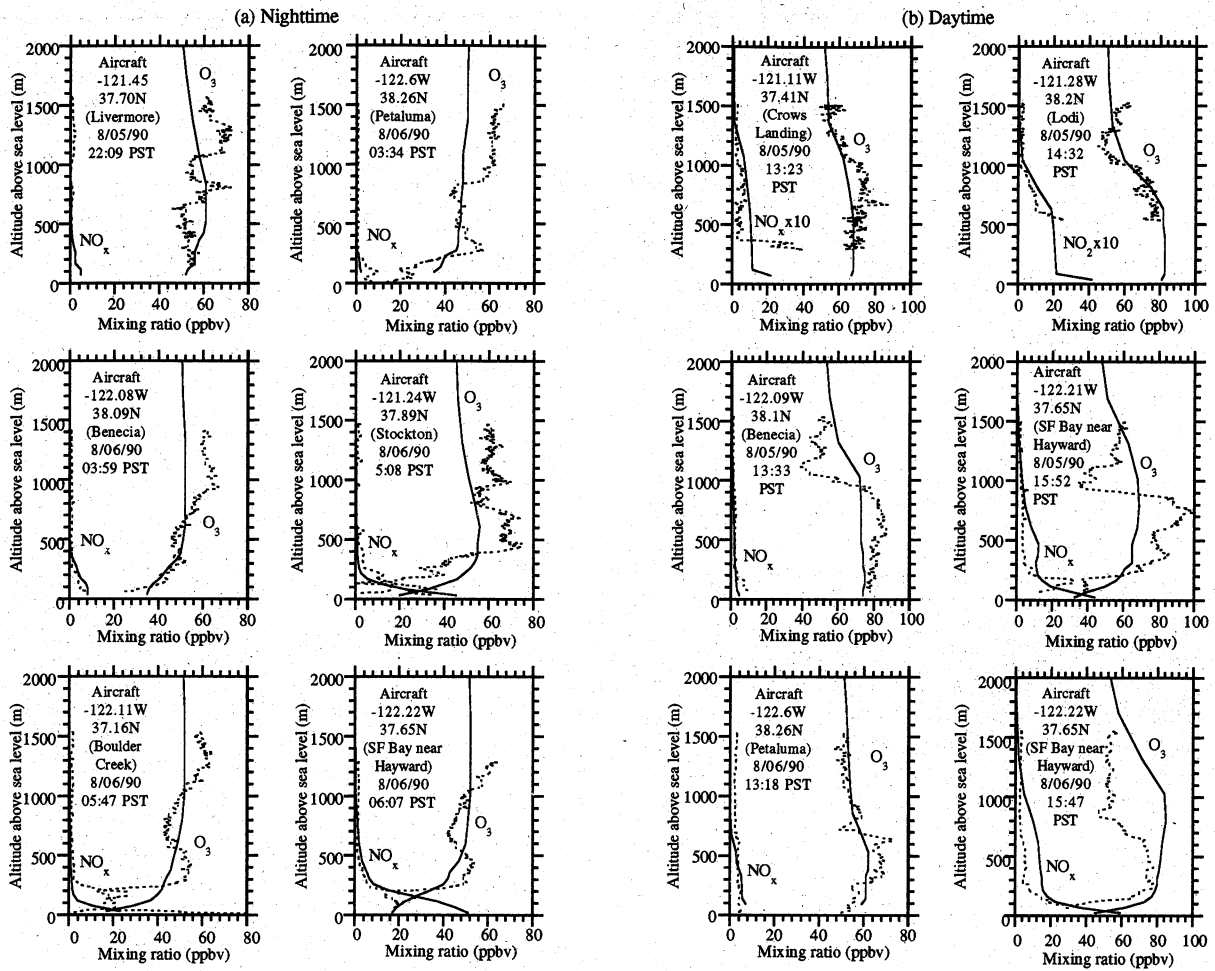
Figure 9. Predicted versus observed (aircraft spiral) vertical profiles of (a) nighttime and (b) daytime ozone and NO$_x$ (NO+NO$_2$). Solid lines are predictions; dashed lines and circles are observations.
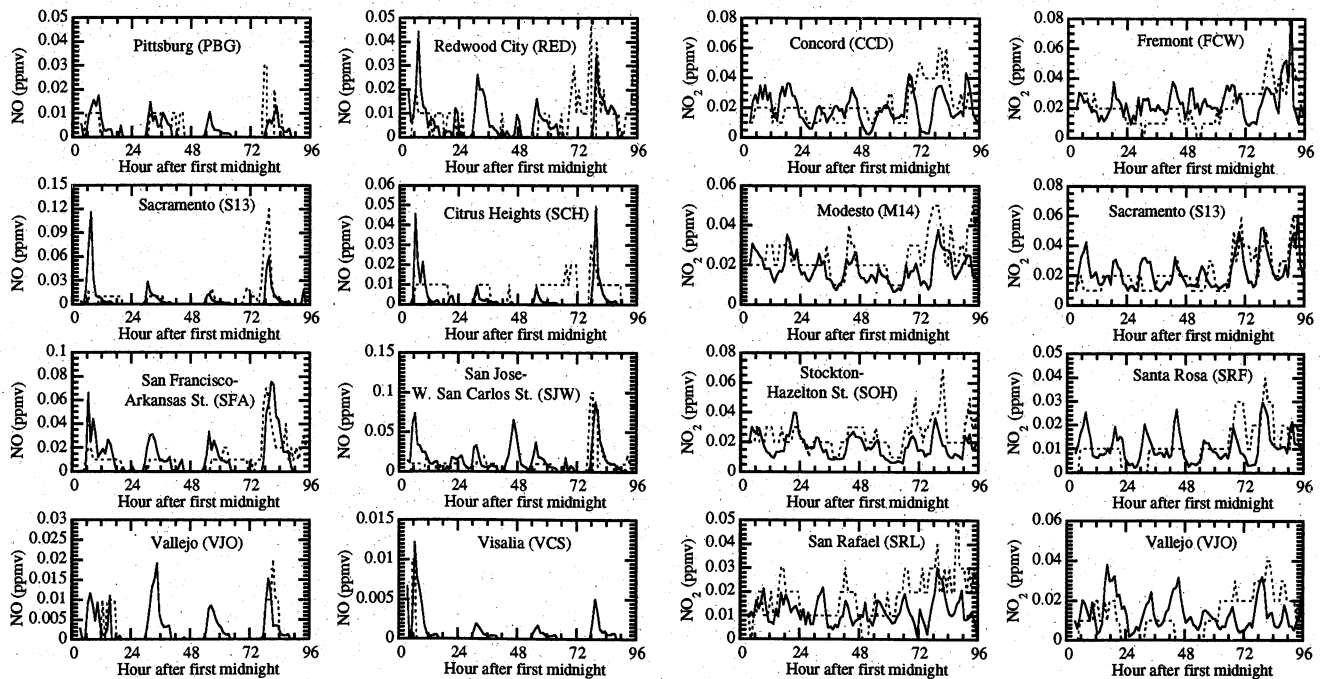
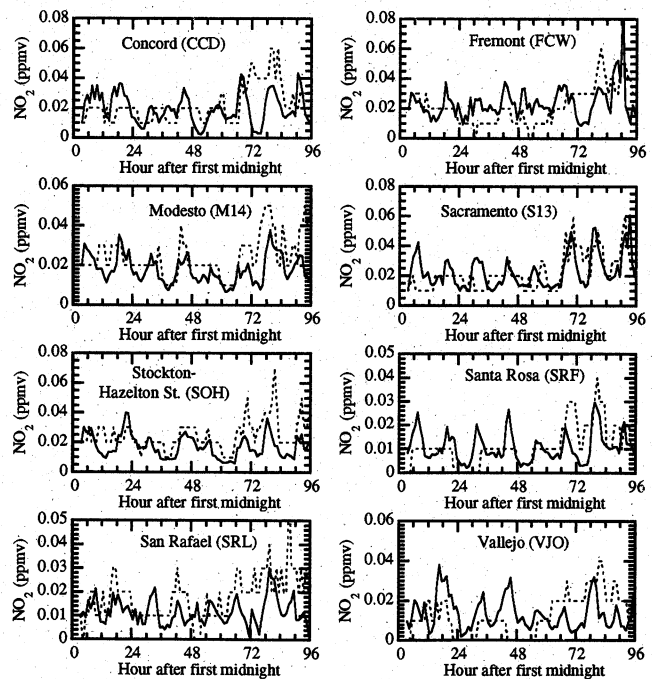**Figure 10.** Same as Figure 3 but for nitric oxide.

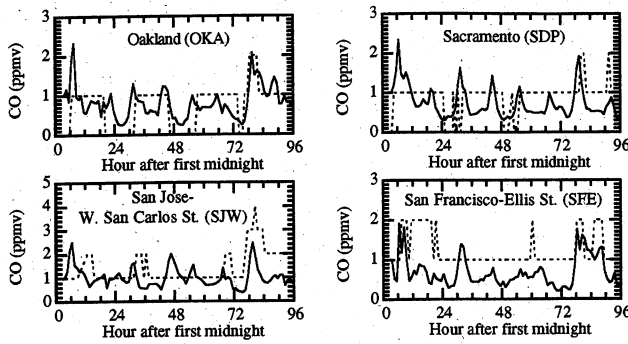**Figure 11.** Same as Figure 3 but for nitrogen dioxide.

Figure 12. Same as Figure 3 but for carbon monoxide.

from a sufficient number of soundings, initialization of soil moisture fields, and treatment of sub-grid-scale soil and land use classes.

Predictions of RH depend on predictions of temperature and water vapor partial pressure; thus, RH is more difficult to predict than is specific humidity or water vapor mixing ratio. Predicting RH correctly is important, not only for obtaining forecasts, but also for predicting ozone, since a major source of OH, required for reactive organic gas breakdown and ozone formation, is $O(^1D)$ reaction with water vapor. RH predictions are also needed for calculating aerosol composition/liquid water content and cloud/fog formation. Aerosols, though, were not simulated in this study.

Figure 4 shows predicted versus observed vertical profiles of temperature and dew point at night, after 48 hours, and in the afternoon, after 84 hours. At all locations, the model predicted a strong nighttime surface inversion. Whereas, observed nighttime surface inversions occurred at most locations, thin observed nighttime mixed layers occasionally formed, such as at King City (KIN) and Livermore (LI2). These thin mixed layers were not predicted. Nighttime temperatures aloft were generally underpredicted. Daytime temperatures aloft were underpredicted, but to a lesser extent. The model predicted the occurrence of observed daytime inversions aloft in some cases, such as at Mariposa (MAR) and Pacheco Pass (PA2), but the inversion base heights were not always predicted exactly. At Livermore (LI2) and Three Rocks (THR), weak observed elevated inversions were not predicted.

Sources of errors in predicted temperature profiles and inversion base heights are incorrect initialization of soil moisture, initialization of atmospheric meteorological
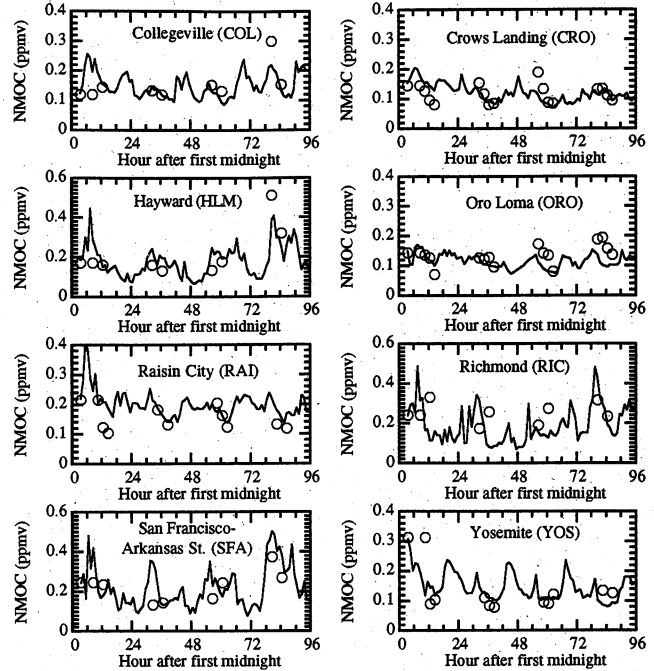

Figure 14. Same as Figure 3 but for nonmethane organic carbon (NMOC).

variables, prediction of surface energy fluxes, and prediction of the movement of a large-scale pressure system. Sources of errors in predicted dew points are incorrect initialization of water vapor outside the region of sounding data, calculation of water vapor fluxes from the ocean and soils, and prediction of winds.

5.2. Wind Speed, Wind Direction, Air Pressure

Wind speeds and directions in northern California depend a lot on the locations of the Pacific high and Aleutian low. During the simulation period, the NCEP reanalysis 500 mbar height over the SARMAP domain increased, and surface air pressures decreased due to enhanced thermal low conditions (e.g., higher surface temperatures). By August 6 at 1600 PST, the 500 mbar height maximum had moved just to the northwest of the NCal domain and had increased to 5975 m from its initial value of about 5900 m. In the largest regional model domain (R1), a 500 mbar height maximum was predicted near
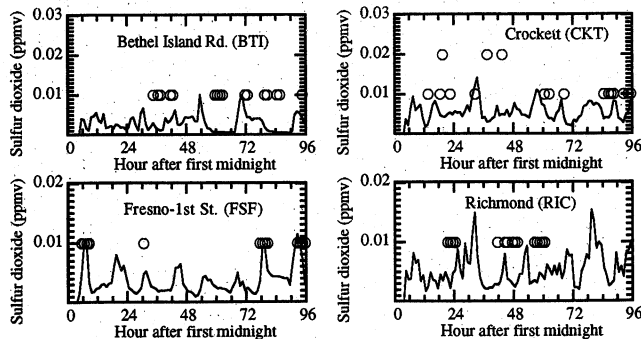

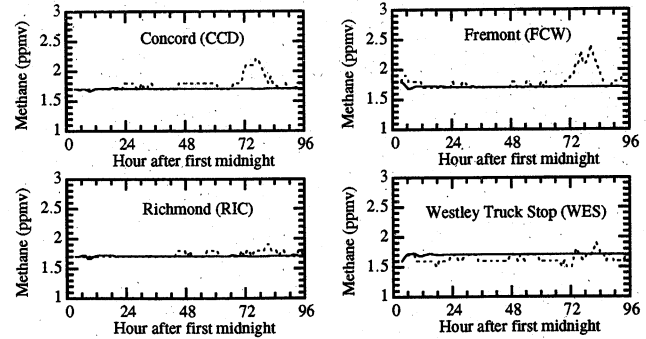**Figure 13.** Same as Figure 3 but for sulfur dioxide.

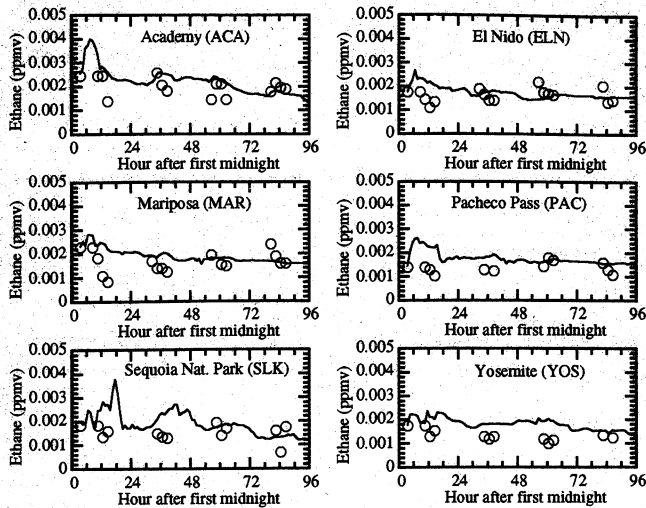**Figure 15.** Same as Figure 3 but for methane.

Figure 16. Same as Figure 3 but for ethane.

this location at the same time. Figure 5 shows that observed surface air pressures decreased by about 4 mbar during the simulation period, and the model (NCal domain) was able to predict these decreases at both Stockton and San Francisco.

Winds in northern California also depend on local factors, such as sea and bay breezes, low-altitude nocturnal jets and eddies in the San Joaquin Valley (particularly near Fresno and on the east side of the valley [e.g., *Smith et al.*, 1981; *Roberts et al.*, 1990]), nighttime drainage flows from the Sierra Nevada Mountains, and convergence/divergence through the Carquinez Straits, Altamont Pass, Cholame Pass, and Pacheco Pass.

Figure 6 shows predicted versus observed near-surface wind speeds and directions. The model predicted the observed strong diurnal wind speed and direction variations at Altamont Pass (ALT) and the strong diurnal wind speed variation at Dixon (DIX). The model captured the observed day/night reversal in wind direction due to nighttime drainage flow at North Fork (NFK), at the base of the Sierra Nevada Mountain Range. It also captured the one-time strong variations in wind direction at Pacheco Pass (PAC), a thoroughfare for pollutants from the
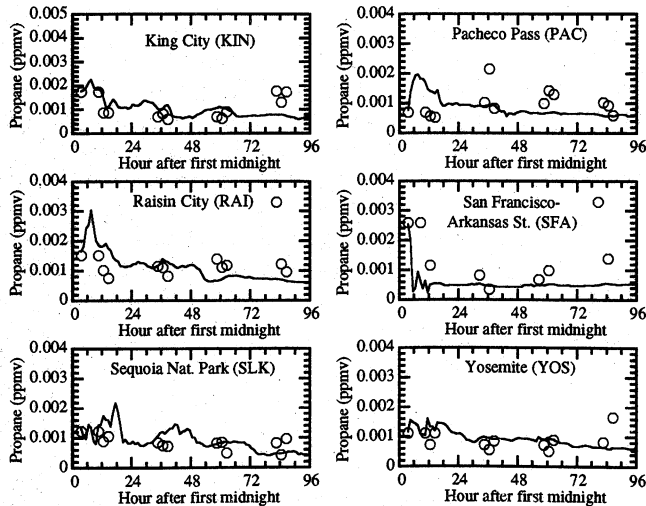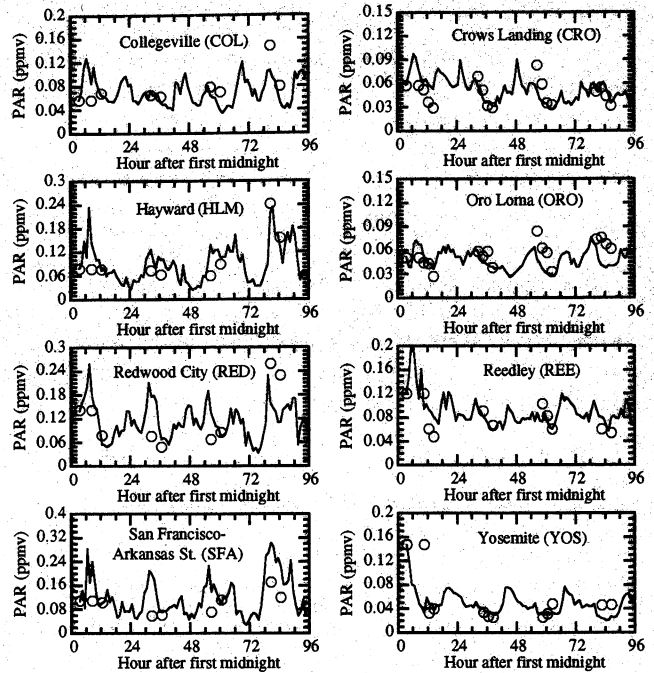

Figure 18. Same as Figure 3 but for paraffins (PAR).

Bay Area to the San Joaquin Valley. The model captured the four strong variations in wind direction at El Patio (EPT), in the southern Santa Clara Valley.

Figure 7 shows predicted versus observed vertical profiles of u- and v-scalar velocities at night, after 48 hours of simulation, and in the afternoon, after 84 hours. The nighttime observation at Stockton (STO) shows the presence of a low, thin nocturnal jet. The model predicted a weaker, thinner jet with a slightly lower peak at the same time. In the day and
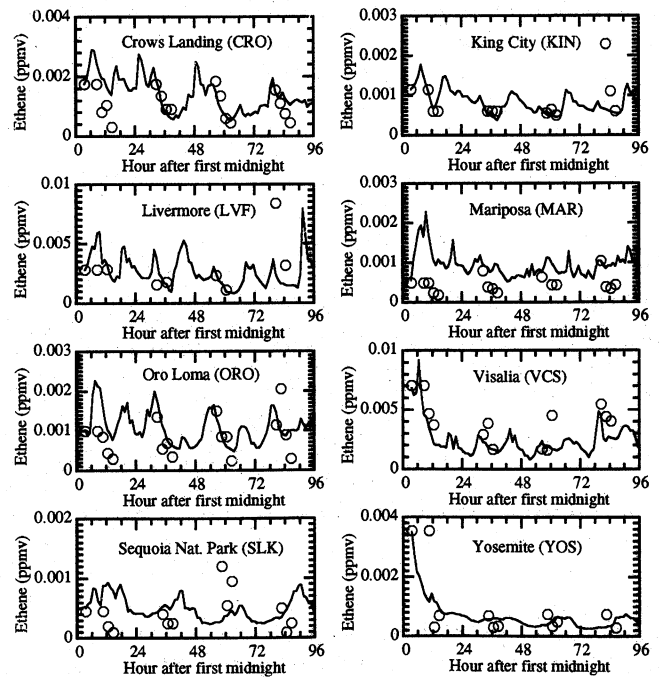

Figure 17. Same as Figure 3 but for propane.

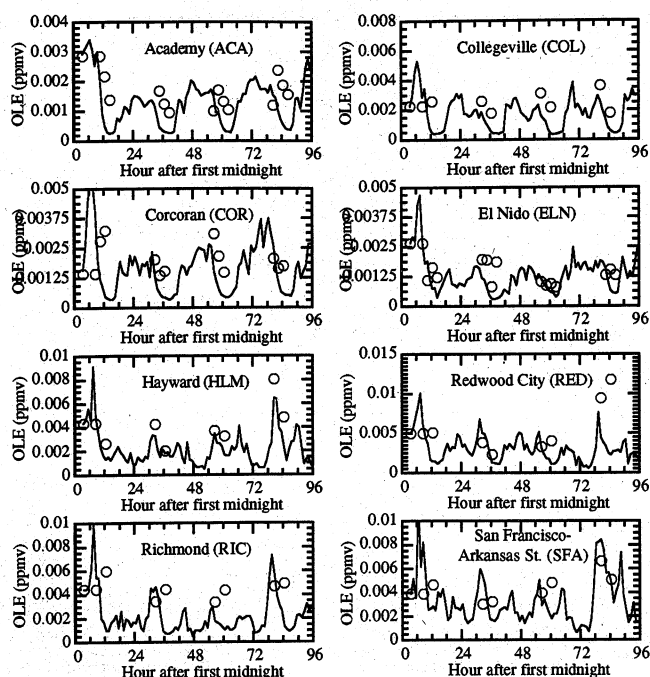**Figure 19.** Same as Figure 3 but for ethene.

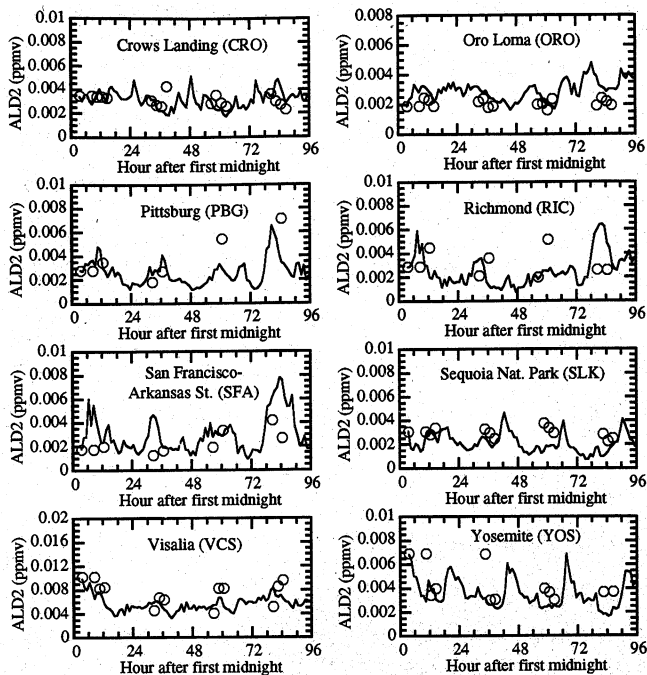Figure 20. Same as Figure 3 but for olefins (OLE).

Figure 22. Same as Figure 3 but for acetaldehyde and higher aldehydes (ALD2).

night wind profiles shown (which were for locations to the east of the San Francisco Bay Area), no significant reversal of flow above the boundary layer back to the coast occurred, indicating that pollutants beyond the Bay Area were unlikely to return back toward the Bay Area when they were injected above the boundary layer. In the Los Angeles basin, flow reversal aloft, driven by hot temperatures in the Mojave desert is a mechanism for recirculating pollutants from beyond the basin back to it in the summer.
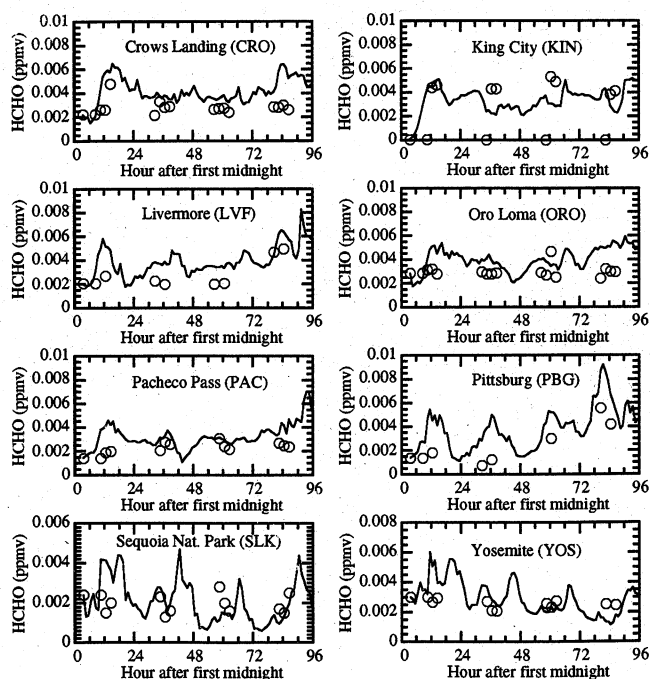

Figure 21. Same as Figure 3 but for formaldehyde (HCHO).

5.3. Near-Surface Ozone

Figure 8 shows time series plots of predicted versus observed near-surface ozone at a variety of sites. The gross error in ozone predictions, normalized over all hourly observations in which ozone mixing ratios exceeded 50 ppbv, was 22.5% (Table 2). For comparison, previous studies of Los Angeles pollution have resulted in prediction accuracies for ozone of 25-35% over a simulation period [e.g., *Harley et al.*, 1993; *Jacobson*, 1997, 1999b]. Peak and average mixing ratios of ozone in Los Angeles are typically higher than those in northern and central California.

To predict observed daytime ozone peaks, it was necessary to initialize the model with observed (from aircraft) elevated ozone layers. When such initialization was not performed, daytime peaks in near-surface ozone were not captured. Although the effect of initialization on accuracy decreased each day, it was still noticeable by the fourth day.

Ozone mixing ratios are affected by emissions of ozone precursors. The SARMAP emissions domain covered the entire NCal (innermost) domain plus an area extending 2° to the south of the domain. All ambient ozone measurements in all nested domains fell within areas covered by the emissions domain. Ozone predictions compared well with observations under a variety of conditions, including conditions of strong diurnal variations (e.g., Altamont [ALT], Collegeville [COL], Modesto [M14], Sacramento [S13], and Stockton-Lodi [STO]), weak diurnal variations but high mixing ratios (e.g., Yosemite [YOS]), and low mixing ratios (e.g., Oakland [OKA], Point Reyes [POR], San Francisco [SFA]). In particular, observed near-surface ozone mixing ratios at coastal sites in northern California were quite low, as seen in Figure 8 for Point Reyes (consistently 30 ppbv), San Francisco (consistently 20 ppbv), and Oakland (consistently 20-30 ppbv). One reason for these low mixing ratios is that winds originating from the ocean carry relatively clean, low-ozone air into these coastal
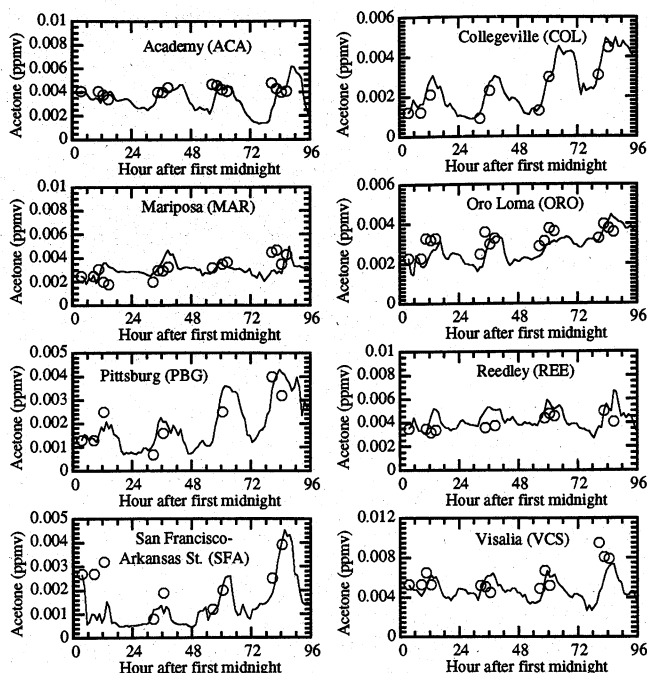
Figure 23. Same as Figure 3 but for acetone.

locations. In addition, the same winds advect emissions of ozone precursors from coastal locations inland, reducing in situ ozone production along the coast. The model was able to reproduce the low mixing ratios at all the coastal locations.

During the simulation period, observed ozone mixing ratios tended to increase. These increases were predicted, for the most part, by the model, except for a few cases (e.g., day 3 at Livermore, Fremont, and San Jose), where abnormally high observed ozone mixing ratios were not replicated. Ozone increases during the period coincided with increases in near-surface temperatures (Figure 3), decreases in surface pressures (Figure 5), and decreases in near-surface wind speeds (Figure 6). The enhanced stagnation of air may have led to the gradual increase in ozone. Since the simulation period ran from a Friday through Monday, it is unlikely that enhanced emissions caused the ozone buildup, particularly on day 3 (Sunday, August 5).

At several locations, ozone was overpredicted at night. Most likely, this was due to too little NO present in the model at night near the measurement station. Alternatively, it may have been due to erroneous nighttime downward mixing of ozone from aloft in the model as a result of a temperature profile that was not stable enough. Such mixing occurs in reality along coastal areas where temperature profiles are often neutral at night (due to fog or high specific humidity) but it should not occur so much inland.

5.4. Elevated Ozone

Aircraft spirals from the SARMAP field campaign indicate the presence of nighttime elevated layers and deep daytime mixed layers of ozone. Some spirals also indicate the presence of daytime elevated ozone layers.

Elevated ozone layers generally form in one of three ways. First, they may form by the destruction of surface ozone. During the afternoon, ozone dilutes uniformly throughout a mixing depth. In the evening, cooling of the ground stabilizes

the air near the surface without affecting the stratification aloft. NO emitted near the surface at night then destroys near-surface ozone. Since air near the surface is stably stratified, ozone aloft does not mix downward to replenish the lost surface ozone. The next day, the mixing depth increases, recapturing the elevated ozone and mixing it downward. *McElroy and Smith* [1993] estimated that daytime downmixing of elevated ozone enhanced surface ozone in certain areas of Los Angeles by 30-40 ppbv above what they would have been due to photochemistry alone. When few nighttime sources of NO exist, elevated ozone layers do not form by this mechanism.

Second, sea breeze circulations themselves can form elevated pollutant layers by lifting pollutant-containing air and injecting it into an inversion layer during its return flow to the ocean. Elevated pollution layers formed by this mechanism have been reported in Tokyo [*Wakamatsu et al.*, 1983], Athens [*Lalas et al.*, 1983], and near Lake Michigan [*Lyons et al.*, 1973; *Fitzner et al.*, 1989]. Third, some of the air rising up a mountain slope following heating of the slope may diverge horizontally, injecting pollutants into an inversion layer. Alternatively, air that rises above an inversion may recirculate down into the inversion, injecting pollutants [e.g., *Lu and Turco*, 1995]. Elevated pollution layers formed by this mechanism have been observed by *Wakimoto and McElroy* [1986] adjacent to the San Bernardino and San Gabriel mountain ranges in Los Angeles.

Figure 9a compares predicted with observed (from aircraft) vertical profiles of ozone and NO_x (=$NO+NO_2$) at several sites during the fourth night of simulation and the third and fourth afternoons of simulation. The night sites are located in the San Joaquin Valley (Stockton), the San Ramon Valley (Livermore), the San Francisco (S.F.) Bay Area (Benecia and the S.F. Bay), north of the Bay Area (Petaluma), and south of the Bay Area (Boulder Creek). In all but one of the nighttime cases, observed surface ozone was reduced or destroyed, most likely due to titration by NO_x, since observed (and modeled) near-surface NO_x mixing ratios in all such cases were higher than those aloft. In the one case where near-surface ozone was not reduced much at night, observed near-surface NO_x mixing ratios were low. The model was able to predict the presence of the observed nighttime elevated ozone layers, although the actual shapes of the predicted profiles were difficult to reproduce.

Figure 9b compares daytime ozone and NO_x profiles with observations from the San Joaquin Valley (Crows Landing and Lodi), the Bay Area (Benecia and the S.F. Bay), and north of the Bay Area (Petaluma). The observed heights to which ozone
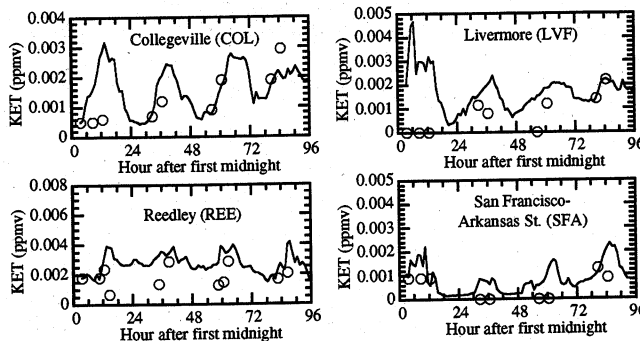

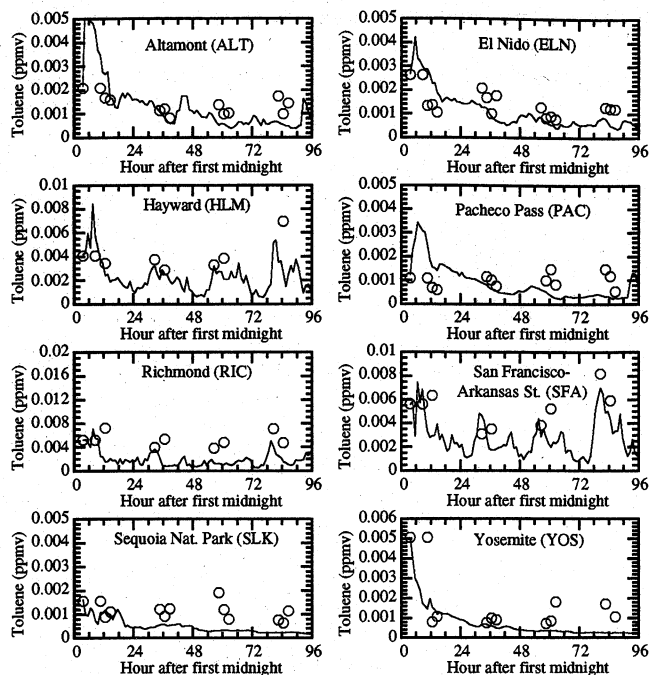**Figure 24.** Same as Figure 3 but for ketones (KET).

Figure 25. Same as Figure 3 but for toluene (TOL).

mixed in the figures can be used as an estimate of pollutant mixing heights. The daytime figures show that the mixing heights at Crows Landing, Lodi, Benecia, and the San Francisco Bay were approximately 1000-1200 m on August 5. The model predicted nearly the correct mixing heights at three of the four locations. Over the S.F. Bay, the model allowed ozone to mix up to 1500 m. On August 6, the model predicted the observed mixing height at Petaluma of about 800-900 m but again overpredicted the mixing height at Hayward.

In four of the six daytime figures shown, ozone mixed relatively uniformly up to the mixing height (although a slight elevated layer formed at Petaluma). Over the S.F. Bay, though, a distinct elevated layer of ozone occurred on the afternoons of August 5 and 6. The location of the S.F. Bay spiral is near the San Mateo Bridge. The west-east bridge and the two south-north freeway arteries on either side of the bridge produce ozone precursors, particularly NO_x and ROGs. Whereas, some ozone aloft over the bay forms in situ, the rest is transported in. A bay breeze circulation forms on both sides of the bay during the day, causing divergence at the surface and convergence aloft near the middle of the bay. The bay breeze circulation, though, is often overpowered, particularly aloft, by stronger large-scale westerly, southwesterly, or northwesterly flow driven by the Pacific High. As a result, most ozone transported over the bay near the San Mateo Bridge probably originates from the peninsula, to the west of the bay.

During the day (and night), NO_x from the bridge and nearby freeway arteries appears to have titrated most of the near-surface ozone over the bridge. Evidence for this includes the high observed NO_x mixing ratios corresponding to the low ozone near the surface on August 5 and 6, as shown in Figure 9b. When daytime near-surface ozone over the bay was destroyed, it was not replenished by ozone aloft for a simple reason. During the day, the bay water temperature is much colder than the air temperature, and a surface inversion is

present. Observed temperature profiles from the aircraft spiral (not shown) verify this and also indicate that the air was stable above the bay to a high altitude. The stability of the air over the bay during the day inhibited downmixing of ozone.

5.5. Nitric Oxide and Nitrogen Dioxide

Figures 10 and 11 show time series plots of predicted versus observed near-surface NO and NO_2, respectively. Observations during SARMAP indicate that NO mixing ratios exhibited near-surface peaks in the early morning. These peaks were frequently, but not always, replicated in the model, but the magnitudes of the peaks were often in error, either due to incorrect emission rates, incorrect predictions of morning-time mixing heights, or incorrect rates of conversion of NO to NO_2. NO_2 predictions were statistically more accurate than were NO predictions (Table 2). NO_2 mixing ratios depend slightly on emissions but more on mixing heights, winds, and chemistry. Observed NO_2 mixing ratios exhibited less of a regular diurnal pattern than did those of NO due to the lesser dependence of NO_2 on morning emissions and greater dependence of NO_2 on chemistry and transport. Because of the irregular pattern of NO_2 mixing ratios, it was difficult for the model to match NO_2 mixing ratios peak for peak.

5.6. Carbon Monoxide and Sulfur Dioxide

Figures 12 and 13 show time series plots of predicted versus observed near-surface CO and SO_2, respectively. The resolution of measurements for these gases were 1 and 0.01 ppmv, respectively. Both gases have emission sources accounted for in the emissions inventory. Their mixing ratios depend on mixing height and transport. SO_2 mixing ratios depend also on rates of gas-to-particle conversion, particularly in fog and cloud drops, which was not accounted for here. Cloud cover, though, was sparse during the SARMAP period, since a high-pressure system dominated. Table 2 indicates that normalized gross errors for CO were less than were those for NO or NO_2, which is not surprising, since CO is less chemically reactive than are NO or NO_2.

5.7. Organic Gases

Figures 14-28 show predicted versus observed near-surface organic gases. Of the gases, methane, ethane, propane, benzaldehyde, and ketones were not explicitly included in the emissions inventory (ethane and propane were included in paraffin and/or olefin carbon-bond-group emissions). Since the only source of ethane and propane and the major source of methane is emissions, the model's ability to predict the mixing ratios of these gases was limited. Yet, methane, ethane, and propane are relatively long-lived; thus, predictions for them were still relatively accurate.

Figure 14 shows that typical observed nonmethane organic carbon (NMOC) mixing ratios ranged from 0.05 to 0.3 ppmv, although values of 0.5 ppmv or more were observed in some locations, such as at Hayward, on August 6 in the afternoon.

Predicted methane mixing ratios (Figure 15) were relatively constant in time due to the absence of methane emission data in the model and the relatively small contribution of chemistry to methane production. Methane measurements indicated abrupt increases at several locations during the night/morning of August 5 to 6. The high mixing ratios may have been due to an abnormal emissions source of methane. The relatively constant modeled mixing ratios of methane over time were a
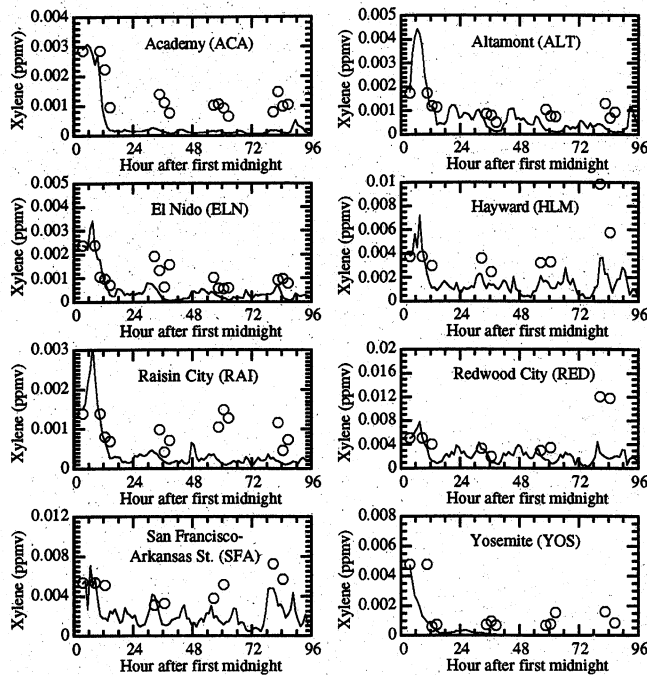
Figure 26. Same as Figure 3 but for xylene (XYL).

good sign that the advection scheme used, described in part 1, conserved the relatively constant mixing ratios of a species, even in the presence of heterogeneous horizontal and vertical wind fields.

Ethane (Figure 16) and propane (Figure 17) mixing ratios in the model were initialized with observations, which varied spatially, but no emissions inventory was available for these gases. Ethane and propane emissions, though, were accounted for through the paraffin (PAR) carbon bond group. Modeled changes in mixing ratios of ethane and propane were due to chemical decay and transport. Since the chemical decay rates of ethane and propane are not fast (e-folding lifetimes of 9.2 and 2.1 days, respectively, when [OH]=5x10^6 molecules cm^{-3}), the lack of large modeled decreases in ethane and propane in Figures 16 and 17 was expected. Mixing ratios of these gases increased in some locations due to transport from locations where mixing ratios were high.

Emission inventories existed for paraffins, ethene, and olefins (Figures 18-20, respectively). The observed total paraffin group (PAR) included ethane and propane. The observed mixing ratios of ethane and propane (Figures 16 and 17, respectively) were <3% those of observed total paraffins (Figure 18). The observed total olefin group (OLE) did not include ethene.

Figures 21-24 show time series plots of formaldehyde, higher aldehydes, acetone, and other ketones. Formaldehyde errors could be due to emissions, chemistry, or meteorological prediction errors. Acetone, whose chemical e-folding lifetime is relatively long (9.6 days when [OH]=5x10^6 molecules cm^{-3}), was predicted reliably. The emission sources of acetone, not included in the inventory, are generally small (about 2% of PAR emissions by mass in Los Angeles during the Southern California Air Quality Study). Emission rates of other ketones are about one-third those of acetone.

Figures 25-27 show time series plots of toluene, xylene, and benzaldehyde, respectively. All three gases are emitted.

Benzaldehyde also has chemical sources, but toluene and xylene do not. Results from one study indicate that xylene and toluene are two of the four most important emitted organic gases in terms of their reactivity in forming ozone [Carter, 1991]. Ethene and acetaldehyde were the other two.

5.8. Isoprene Effect on Ozone at National Parks

Observed isoprene mixing ratios (Figure 28) were higher (0.002-0.006 ppmv) in Sequoia and Yosemite National Parks than in other locations (<0.001 ppmv) in the SARMAP domain. Observed NMOC mixing ratios in the parks ranged from 0.06 to 0.3 ppmv; thus, isoprene never comprised more than 10% of the total NMOCs and usually closer to 2-3%. Although isoprene products or nonisoprene biogenic hydrocarbons may have made up an additional portion of the observed NMOC at Sequoia and Yosemite, SARMAP data indicate that a large portion of NMOC was anthropogenic.

Observed near-surface ozone mixing ratios at Sequoia and Yosemite varied from 0.04 to 0.1 ppmv during the simulation period, with peaks occurring on the afternoon of the first day of simulation at both locations (0.099 and 0.098 ppmv, respectively). A comparison of modeled with observed ozone at Yosemite is shown in Figure 8.

Sensitivity tests were run to estimate the effect of anthropogenic gases and biogenic hydrocarbons on peak ozone in these parks. For the first test, all initial isoprene (surrogate for biogenic hydrocarbons) was removed from all domains, and all isoprene emissions were turned off. Isoprene emissions in the SARMAP inventory between August 3 and 6 were 418, 618, 1000, and 1080 tons per day, respectively. The increase in emissions each day was due to hotter temperatures each day. For the second test, all initial gas mixing ratios were set to background values and all anthropogenic gas and isoprene emissions were turned off. The difference between ozone in the parks from this simulation and that from the no-isoprene case was assumed to be ozone resulting from anthropogenic gases.

Results indicate that on the afternoon of the first day of simulation, an estimated 57 and 54% of peak ozone produced at Sequoia and Yosemite, respectively, was anthropogenic in origin, 3 and 4%, respectively, was biogenic-hydrocarbon in
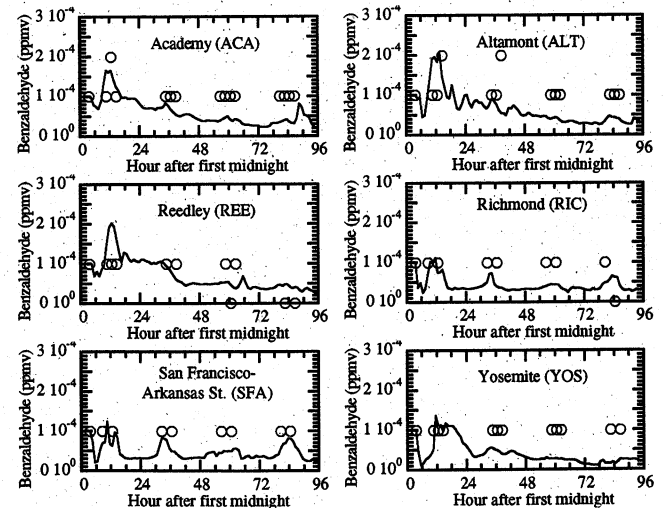

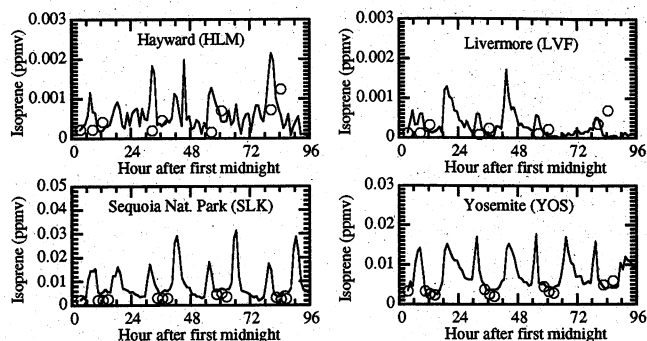**Figure 27.** Same as Figure 3 but for benzaldehyde.

Figure 28. Same as Figure 3 but for isoprene.

origin, and the rest was background. If the higher emissions rates of isoprene that occurred on subsequent days had occurred on the first day of simulation, the contribution of biogenic hydrocarbons to ozone on the first day would have increased to 8 and 11% of total ozone at Sequoia and Yosemite, respectively. In sum, it is estimate that, of the 0.1 ppmv peak ozone at the two parks, about 47-57% was anthropogenic in origin, 11-3% was biogenic-hydrocarbon in origin, and the rest (about 40%) was background. These results depend a lot on the emissions inventory.

5.9. Multiple Gases at Individual Locations

Figures 29 and 30 show predictions versus observations of 14 gases and bond groups at San Jose and Fresno, obtained from the innermost nested domain of the nested simulation. These locations were chosen, because they were particularly polluted. Whereas, errors can be seen, predictions were generally comparable with observations at both locations. Noticeable errors were those for ozone on the third day at San Jose and Fresno. These underpredictions may have been due to an unusual downmixing of elevated ozone to the surface. Since mixing ratios of most other gases did not increase during the afternoon of the third day, it seems unlikely that a thin mixing height or enhancement of emissions occurred during this time.

6. The Effects of Nesting

Table 2 compares statistics from the innermost nested domain of the nested simulation with those from the outer regional domains from the same simulation and with the only domain of the nonnested simulation. For many parameters (including temperature, air pressure, wind speed, and ozone, for example), accuracy improved from the coarsest to finest regional domains. In some cases (e.g., RH, CO, SO_2), results from one of the coarser grids were slightly better than those from the NCal grid.

The difference in ozone gross errors between the finest domain (NCal) and the next-finest regional domain (R3) was small enough (22.5% versus 22.9%) to suggest that the 15 x 20 km spacing of the R3 grid might be sufficient for predicting ozone reasonably. The differences in errors for temperatures (1.02% versus 1.20%) and RHs (26.2% versus 29.1%) were larger. Since computer time scales relatively linearly with the number of nested domains used (part I gives absolute timings), the computational cost of using five domains was a factor of four greater than that from using one domain.

Between the NCal and the R3 domains, the normalized bias for ozone became slightly less negative, but between the R3 and the R1 domains, the bias became more negative. This suggests that beyond a certain grid spacing, the coarser the domain resolution, the lower the mixing ratio of predicted ozone. The phenomenon is of interest, because several studies have examined the effects of domain resolution and/or dilution on ozone mixing ratios, ozone production, or ozone production efficiency [e.g., Chatfield and Delany, 1990; Sillman et al., 1990; Jang et al., 1995; Poppe et al., 1998; Hilst, 1998; Liang and Jacobson, 2000]. Jang et al. [1995], for example, found that increasing domain resolution could increase or decrease modeled ozone at specific locations. Here, finer resolution resulted in higher ozone mixing ratios over the SARMAP domain, except between domains R3 and NCal.

Table 2 indicates that ozone prediction accuracy in the innermost nested domain was about 2.8% better than that obtained when no nesting was used. Prediction-accuracy
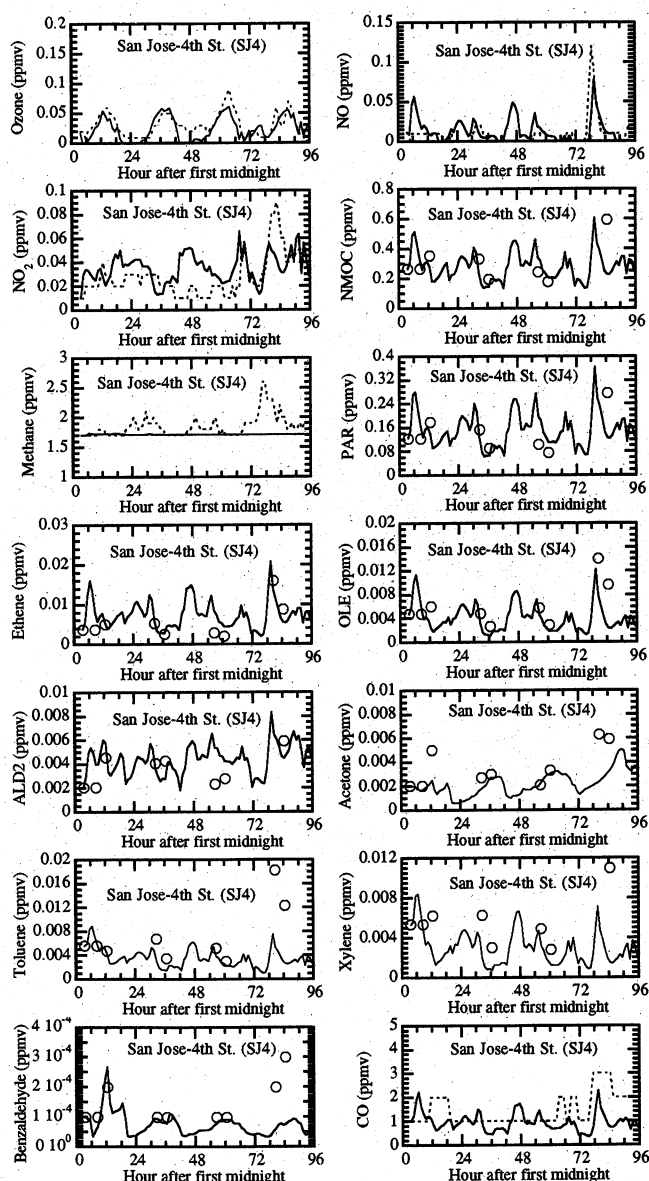

Figure 29. Same as Figure 3 but for 15 gases and bond groups at San Jose, California.
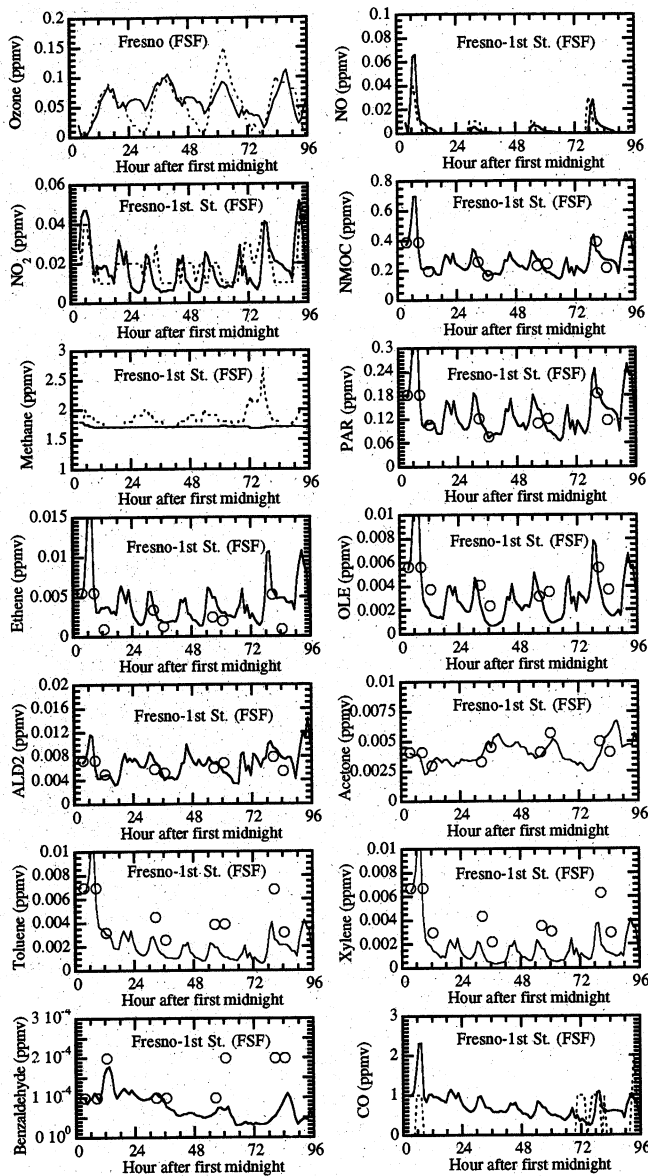
Figure 30. Same as Figure 3 but for 15 gases and bond groups at Fresno, California.

improvements of temperatures, RHs, winds, air pressures, and other gases were also modest. Figures not shown indicate that nesting improved predictions of elevated winds more than of surface winds. The reason may be that surface winds (e.g., sea, land, mountain, and valley breezes) appear to be controlled mostly by local forcings, such as boundary layer temperature and pressure gradients, which depend on land- and ocean-surface processes. Elevated winds are controlled more by a combination of large-scale pressure gradients and local forcings. Without nesting, large-scale forcings were not represented well; thus, elevated wind predictions eroded rapidly. Surface winds, though, were represented well even without nesting.

Improvements in temperatures aloft due to nesting were less noticeable than were improvements in winds aloft. Part of the reason may be that temperatures aloft are more sensitive to land-surface processes than are winds aloft.

7. Conclusion

A global- through urban-scale prognostic air pollution/weather forecast model was applied to the SARMAP field campaign of August 3-6, 1991. Near-surface predictions of temperatures, RHs, and ozone were the most accurate parameters compared. For the most part, finer-resolution grid spacing produced better predictions than did coarser-resolution spacing. Also, the finer the grid spacing, the lesser the underprediction of ozone. Nesting the model through the global scale improved meteorological and air pollutant predictions in comparison with a nonnested simulation, but improvements were not large.

The model simulated observed nighttime ozone layers aloft and daytime ozone mixed layers in the San Joaquin Valley and San Francisco Bay Area. It also replicated the occurrence of elevated daytime ozone layers over the San Francisco Bay near Hayward. These layers may have been caused by titration of surface ozone by NO_x from local freeways and a bridge. The model was used to estimate that of the 0.1 ppmv peak ozone at Sequoia and Yosemite National Parks, about 47-57% was anthropogenic in origin, 11-3% was biogenic-hydrocarbon in origin, and the rest was background.

References

Bingham, G. E., D. K. Zhou, B. Y. Bartschi, G. P. Anderson, D. R. Smith, J. H. Chetwynd, and R. M. Nadile, Cryogenic Infrared Radiance Instrumentation for Shuttle (CIRRIS 1A) Earth limb spectral measurements, calibration, and atmospheric O_3, HNO_3, CFC-12, and CFC-11 profile retrieval, *J. Geophys. Res.*, 102, 3547-3558, 1997.

Blumenthal, D. L., Field study plan for the San Joaquin Valley Air Quality Study (SJVAQS) and the Atmospheric Utility Signatures, Predictions, and Experiments (AUSPEX) Program, final report, Calif. Air Resour. Board, STI-98020-1241-FR, Sacramento, 1993.

Carter, W. P. L., Development of ozone reactivity scales for volatile organic compounds, *EPA-600/3-91-050*, U.S. Environ. Prot. Agency, Res. Triangle Park, N. C., 1991.

Chang, J. S., S. Jin, Y. Li, M. Beauharnois, C.-H. Lu, H.-C. Huang, S. Tanrikulu, and J. DaMassa, The SARMAP Air Quality Model, final report, Air Resour. Board, Calif Environ. Prot. Agency, Sacramento, 1997.

Chatfield, R. B., and A. C. Delany, Convection links biomass burning to increased tropical ozone: However, models will tend to overpredict O_3, *J. Geophys. Res.*, 95, 18,473-18,488, 1990.

Dabdub, D., L. L. DeHaan, and J. H. Seinfeld, Analysis of ozone in the San Joaquin Valley of California, *Atmos. Environ.*, 33, 2501-2514, 1999.

DaMassa, J., S. Tanrikulu, K. Magliano, A. J. Ranzieri, and E. Niccum, Performance evaluation of SAQM in central California and attainment demonstration for the 3-6 August 1990 ozone episode, Calif. Air Resour. Board, Sacramento, 1996.

Fitzner, C. A., J. C. Schroeder, R. F. Olson, and P. M. Tatreau, Measurement of ozone levels by ship along the eastern shore of Lake Michigan, *J. Air Pollut. Control Assoc.*, 39, 727-728, 1989.

Harley, R. A., A. G. Russell, G. J. McRae, G. R. Cass, and J. H. Seinfeld, Photochemical modeling of the Southern California Air Quality Study, *Environ. Sci. Technol.*, 27, 378-388, 1993.

Hilst, G. R., Segregation and chemical reaction rates in air quality models, *Atmos. Environ.*, 32, 3891-3895, 1998.

Jackman, C. H., E. L. Fleming, S. Chandra, D. B. Considine, and J. E. Rosenfield, Past, present, and future modeled ozone trends with comparisons to observed trends, *J. Geophys. Res.*, 101, 28,753-28,767, 1996.

Jacob, D. J., et al., Origin of ozone and NOx in the tropical troposphere: A photochemical analysis of aircraft observations over the South Atlantic basin, *J. Geophys. Res., 101*, 24,235-24,250, 1996.

Jacobson, M. Z., Development and application of a new air pollution modeling system, part III, Aerosol-phase simulations, *Atmos. Environ., 31*, 587-608, 1997.

Jacobson, M. Z., Effects of soil moisture on temperatures, winds, and pollutant concentrations in Los Angeles, *J. Appl. Meteorol., 38*, 607-616, 1999.

Jacobson, M. Z., GATOR-GCMM: A global- through urban-scale air pollution and weather forecast model, 1, Design and treatment of subgrid soil, vegetation, roads, rooftops, water, sea ice, and snow, *J. Geophys. Res.*, this issue.

Jang, J. C. C., H. E. Jeffries, and S. Tonnesen, Sensitivity of ozone to model grid resolution II, Detailed process analysis for ozone chemistry, *Atmos. Environ., 29*, 3101-3114, 1995.

Lagarias, J. S., and W. W. Sylte, Designing and managing the San Joaquin Valley air quality study. *J.Air Waste Manage. Assoc., 41*, 1176-1179, 1991.

Lalas, D. P., D. N. Asimakopoulos, D. G. Deligiorgi, and C. G. Helmis, Sea-breeze circulation and photochemical pollution in Athens, Greece, *Atmos. Environ., 17*, 1621-1632, 1983.

Liang, J., and M. Z. Jacobson, Effects of subgrid mixing on ozone production in a chemical model: Dilution may reduce bulk ozone production efficiency, *Atmos. Environ., 34*, 2975-2918, 2000.

Lu, C.-H., and J. S. Chang, On the indicator-based approach to assess ozone sensitivities and emissions features, *J. Geophys. Res., 103*, 3453-3462, 1998.

Lu, R., and R. P. Turco, Air pollutant transport in a coastal environment, II, Three-dimensional simulations over Los Angeles basin, *Atmos. Environ., 29*, 1499-1518, 1995.

Lyons, W. A., and L. E. Olsson, Detailed mesometeorological studies of air pollution dispersion in the Chicago lake breeze, *Mon. Weather Rev., 101*, 387-403, 1973.

Magliano, K. L., Summary of SARMAP emissions modeling. Tech. Support Div., Calif. Air Resour. Board, Sacramento, 1994.

McElroy, J. L., and T. B. Smith, Creation and fate of ozone layers aloft in Southern California, *Atmos. Environ., 27(A)*, 1917-1929, 1993.

National Centers for Environmental Prediction (NCEP), 2.5 degree global final analyses, distributed by the Data Support Section, 1999.

Poppe, D., R. Koppmann, and J. Rudolph, Ozone formation in biomass burning plumes: Influence of atmospheric dilution, *Geophys. Res. Lett., 25*, 3823-3826, 1998.

Pun, B. K., J.-F. Louis, P. Pai, C. Seigneur, S. Altshuler, and G. Franco, Ozone formation in California's San Joaquin Valley: A critical assessment of modeling and data needs, *J. Air Waste Manage. Assoc., 50*, 961-971, 2000.

Ranzieri, A. J., and R. H. Thuillier, SJVAQS and AUSPEX: A collaborative air quality field measurement and modeling program, edited by P. A. Solomon, Plann. and Managing Reg. Air Qual., A. F. Lewis, New York, 1994.

Roberts, P. T., T. B. Smith, C. G. Lindsey, and W. R. Knuth, Analysis of San Joaquin Valley Air Quality and Meteorology, *Sonoma Technol. Rep. STI-98101-1006-FR*, Santa Rosa, Calif., 1990.

Seaman, N. L., D. R. Stauffer, and A. M. Lario-Gibbs, A multiscale four dimensional data assimilation applied in the San Joaquin Valley during SARMAP, Part I, Modeling design and basic performance characteristics, *J. Appl. Meteorol., 34*, 1739-1761, 1995.

Sillman, S., J. A. Logan, and S. C. Wofsy, A regional scale model for ozone in the United States with subgrid representation of urban and power plant plumes, *J. Geophys. Res., 95*, 5731-5748, 1990.

Singh, H. B., et al., Reactive nitrogen and ozone over the western Pacific: Distribution, partitioning, and sources, *J. Geophys. Res., 101*, 1793-1808, 1996.

Smith, T. B., D. E. Lehrman, D. D. Reible, and F. H. Shar, The origin and fate of airborne pollutants within the San Joaquin Valley: Extended summary and special analysis topics, *Tech. rep. MRI FR-1838*, Meteorol. Research, Inc., Altadena, Calif. and Calif. Inst. of Technol., Pasadena, Calif., 1981.

Solomon, P. A., and R. H. Thuillier, SJVAQS/SUSPEX/SARMAP 1990 Air Quality Field Measurement Project, vol. II, Field measurement characterization. PG&E Rep. 009.2-94.1, San Ramon, Calif., 1995.

Wakamatsu, S., Y. Ogawa, K. Murano, K. Goi, and Y. Aburamoto, Aircraft survey of the secondary photochemical pollutants covering the Tokyo metropolitan area, *Atmos. Environ., 17*, 827-836, 1983.

Wakimoto, R. M. and J. L. McElroy, Lidar observation of elevated pollution layers over Los Angeles, *J. Clim. Appl. Meteorol., 25*, 1583-1599, 1986.

Zhou, D. K., G. E. Bingham, B. K. Rezai, G. P. Anderson, D. R. Smith, and R. M. Nadile, Stratospheric CH_4, N_2O, H_2O, NO_2, N_2O_5, and $ClONO_2$ profiles retrieved from Cryogenic Infrared Radiance Instrumentation for Shuttle (CIRRIS 1A)/STS 39 measurements, *J. Geophys. Res., 102*, 3559-3573, 1997.

M. Z. Jacobson, Department of Civil and Environmental Engineering, Terman Engineering Center, Room M-13, Stanford University, Stanford, CA 94305-4020. (e-mail: jacobson@ce.stanford.edu)